

Towards Nanoscale and Element-Specific Lattice Temperature Measurements using Core-Loss Electron Energy-Loss Spectroscopy

Levi D. Palmer,¹ Wonseok Lee,¹ Javier Fajardo, Jr.,² A. Alec Talin,² Thomas E. Gage,^{3,*} Scott K. Cushing^{1,*}

¹*Division of Chemistry and Chemical Engineering, California Institute of Technology, Pasadena, CA 91125, USA*

²*Sandia National Laboratories, Livermore, California 94551, USA*

³*Center for Nanoscale Materials, Argonne National Laboratory, Lemont, IL 60439, USA*

*Correspondence to [Thomas E. Gage](#) & [Scott K. Cushing](#)

ABSTRACT

Measuring nanoscale local temperatures, particularly in vertically integrated and multi-component systems, remains challenging. Spectroscopic techniques like X-ray absorption and core-loss electron energy-loss spectroscopy (EELS) are sensitive to lattice temperature, but understanding thermal effects is nontrivial. This work explores the potential for nanoscale and element-specific core-loss thermometry by comparing the Si L_{2,3} edge's temperature-dependent redshift against plasmon energy expansion thermometry (PEET) in a scanning TEM. Using density functional theory (DFT), time-dependent DFT, and the Bethe-Salpeter equation, we *ab initio* model both the Si L_{2,3} and plasmon redshift. We find that the core-loss redshift is due to bandgap reduction from electron-phonon renormalization. Our results indicate that despite lower core-loss signal intensity and thus accuracy compared to PEET, core-loss thermometry still has important advantages. Specifically, we show that the Varshni equation easily interprets the core-loss redshift, which avoids plasmon spectral convolution for PEET in complex materials. We also find that core-loss thermometry is more accurate than PEET at modeling thermal lattice expansion unless the temperature-dependent effective mass and dielectric constant are known. Furthermore, core-loss thermometry has the potential to measure nanoscale heating in multi-component materials and stacked interfaces with elemental specificity at length scales smaller than the plasmon's wavefunction.

INTRODUCTION

Measurements of temperature with nanoscale resolution are critical for understanding and managing thermal gradients and is crucial for optimizing electronic, photonic, and energy conversion and storage devices. During operation, local thermal variations can lead to nanoscale effects that dictate device performance. For example, the end of Dennard scaling for transistors and the inability to effectively remove heat has limited device density and clock speed in central processing units since the early 2000s.¹ The performance, reliability and aging of semiconductor devices used in transportation, renewable energy systems, and the electric grid to switch high power critically depends on adequate thermal control.² On the other hand, modest temperature increases in semiconductor based photocatalytic systems have recently been reported to substantially improve solar hydrogen generation, suggesting that nanoscale hot spots could be engineered to enhance catalytic active sites.^{3,4} To understand how local thermal distribution can be

either detrimental or beneficial in these various applications requires the ability to measure temperature *in situ* and relate these measurements to local composition and microstructure.

Plasmon energy expansion thermometry (PEET) is one technique theoretically capable of imaging sub-nm local temperatures.^{5–10} PEET is performed by measuring the shift in a material's volume plasmon with temperature. Thermal lattice expansion shifts the plasmon according to the free electron model as described in the next section. PEET in a scanning TEM (STEM) with electron energy-loss spectroscopy (EELS) has been used to image nanoscale temperatures and thermal lattice expansion coefficients for nanoparticles, membranes, and two-dimensional materials.^{5–11} However, recent studies show that the volume plasmon can vary with sample thickness.¹² Artifacts can also obscure accurate PEET temperature measurements because the plasmon energy varies quadratically with momentum.^{13–15} Local strain variations can exceed the thermal expansion percentage, especially at junctions and interfaces.¹⁶ PEET also has difficulty measuring temperature in materials with small thermal expansion coefficients because the plasmon energy shifts <0.1 meV/K. PEET's challenges necessitate additional spectromicroscopy tools capable of measuring nanoscale temperature distributions for a wide variety of materials.

We propose a core-loss thermometry alternative to PEET. Core-loss thermometry can probe the lattice temperature because core-level spectroscopies, like X-ray absorption and core-loss EELS, measure a material's valence states. Extended X-ray absorption fine structure (EXAFS) spectra have previously been used to quantify lattice temperatures, but EXAFS requires high-energy X-rays and edges that are difficult to resolve with core-loss EELS, limiting spatial resolution.^{17,18} Studies using ultrafast and photoexcited X-ray spectroscopy have found that core-level edges redshift with temperature, but the exact redshift mechanism has yet to be quantitatively analyzed.^{19,20} We aim to understand and predict this temperature-dependent redshift using accurate electronic structure models to develop core-loss thermometry.

Specifically, we use *in situ* STEM-EELS heating at low magnifications to map the temperature-dependent low- and core-loss EEL spectra of a 183 ± 33 nm crystalline Si membrane with inherent curvature and native oxide. We test the accuracy of PEET across the curved membrane and simultaneously perform core-loss thermometry to relate the Si volume plasmon energy shift to changes in the $L_{2,3}$ edge ($2p \rightarrow 3s+d$ core electron transitions). We further incorporate analytic theory for both the plasmon and $L_{2,3}$ edge using density functional theory (DFT), linearized time-dependent DFT (TDDFT), and the Bethe-Salpeter equation (BSE). The combination of theory and measurements quantifies the temperature-dependent core-loss EELS. We find that the core-loss spectrum redshifts according to the reduction of silicon's temperature-dependent bandgap due to lattice expansion and electron-phonon renormalization as predicted by the Varshni equation.^{21,22} Interpreting this core-loss redshift is, therefore, easier than PEET for materials and devices with multiple plasmons and low-loss peaks. We also find core-loss thermometry to be more accurate than PEET at measuring the thermal expansion coefficient when the temperature-dependent valence band effective mass and dielectric constant are unknown. Core-loss thermometry could ultimately measure element-specific lattice temperatures at the nanoscale during operando or ultrafast measurements.

RESULTS

Figure 1 depicts the experimental setup used to measure PEET and core-loss thermometry. When integrated with STEM-EELS, PEET can accurately map the plasmon energy shift (**Figure 1a**). The

measured 183 ± 33 nm thick Si membrane with native oxide was prepared by mechanically polishing and Ar-ion thinning $\sim 20,000 \Omega \cdot \text{cm}$ Si ($\sim 2.2 \cdot 10^{11}$ intrinsic N_D). The inset shows that the Si plasmon energy redshifts linearly with temperature without hysteresis across the film.

The volume plasmon energy (E_p) redshifts due to thermal lattice expansion according to the free electron model in Equation 1:

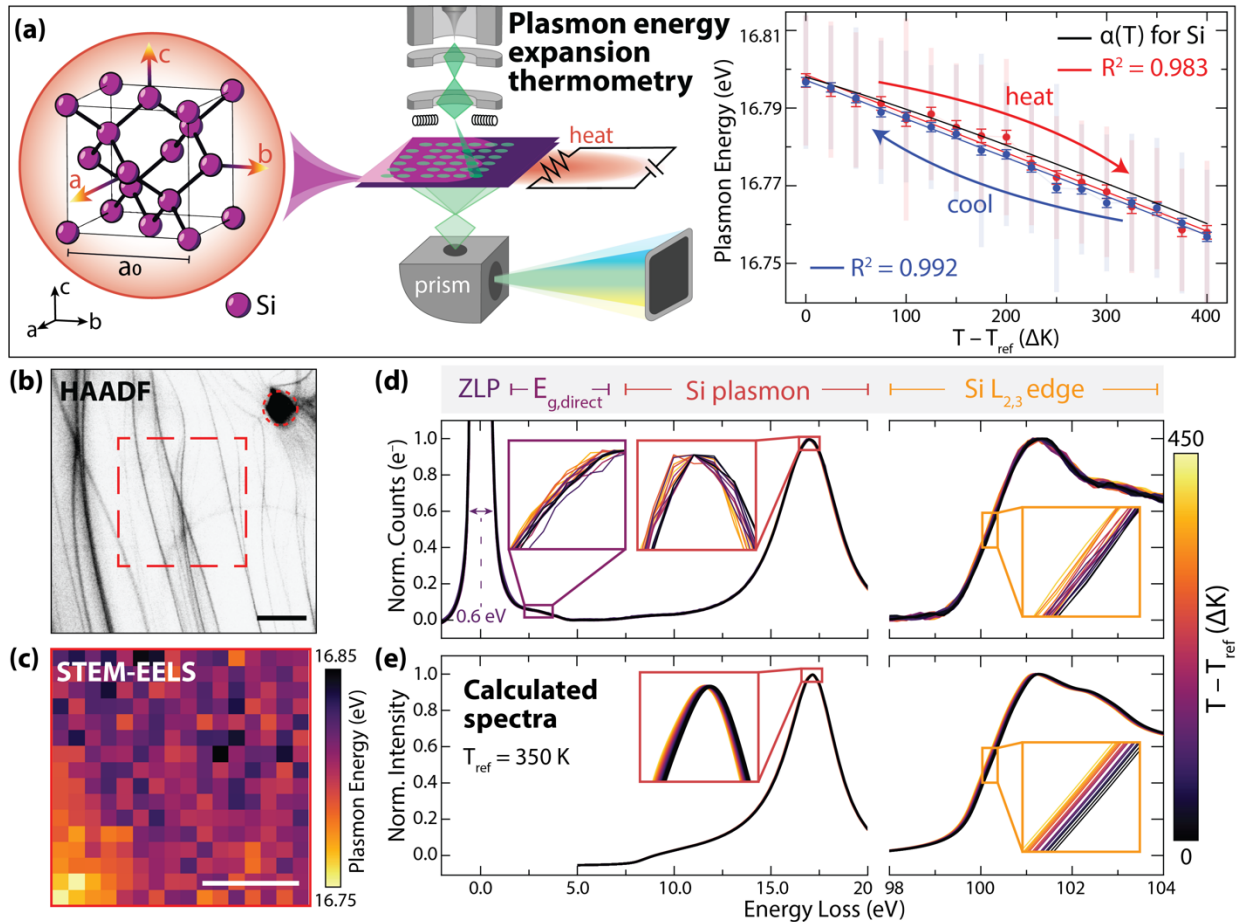


Figure 1. Temperature-dependent scanning TEM electron energy-loss spectroscopy (STEM-EELS). (a) Plasmon energy expansion thermometry: thermal expansion of crystalline Si due to resistive heating is measured by STEM-EELS using a cold field-emission gun. The inset depicts the plasmon energy shift while heating and cooling a Si membrane as compared to the plasmon energy calculated using the T-dependent thermal expansion coefficient. Shaded bars are the plasmon energy standard deviation in each STEM image, error bars were calculated using reduced χ^2 . $T_{\text{ref}} = 350$ K. (b) A dark-field survey of the membrane at T_{ref} . The dashed red square represents (c) the STEM-EELS acquisition region, and the red circle is a defect used for imaging alignment. Scale bars are $5 \mu\text{m}$. False coloration represents hot colors as “warmer” sample regions, and center-of-mass fitting was used to determine the plasmon energy. See supplementary GIFs for temperature-dependent dark-field and plasmon energy scans. (d) Temperature-dependent spectra of the Si membrane collected using dualEELS and aligned to the zero-loss peak (ZLP). Each spectrum is an average of spectra in each 16×16 pixel STEM-EELS image. The direct bandgap ($E_{g,\text{direct}}$) and Si $L_{2,3}$ edge are power-law background-subtracted. (e) Calculated Si EEL spectra modeled over a range of expanded lattice parameters using the temperature-dependent, isotropic thermal expansion coefficient of Si [ref. 23]. The unit cell’s energy-optimized lattice parameter (a_0) was 10.33 Bohr (5.47 \AA). A scissor shift was applied to the calculated Si $L_{2,3}$ edge according to the temperature-dependent band gap [ref. 21], and the edge was broadened by an energy-dependent Lorentzian broadening.

$$E_p(T) = \hbar\omega_p(T) = \hbar \sqrt{\frac{n(T)e^2}{m_{\text{eff}}\epsilon_{\infty}}} \quad (1)$$

As the Si lattice expands, the carrier density $n(T)$ decreases (ϵ_{∞} , e , and m_{eff} are the media's dielectric constant, electron charge, and valence band effective mass, respectively). The electron's temperature-dependent effective mass and dielectric constant vary with temperature but are typically ignored by PEET studies by interpreting the *relative* change in the plasmon energy according to the thermal expansion coefficient ($\alpha(T)$) using Equation 2:

$$E_p(T) = E_{p0} * \left(1 - \frac{3}{2} * \int_{T_{\text{ref}}}^T \alpha(T) dT \right) \quad (2)$$

Here, E_{p0} is the plasmon energy at the reference temperature (T_{ref}) and $\alpha(T)$ is the temperature-dependent thermal expansion coefficient of Si.²³ Equation 2 was used to calculate the temperature-dependent plasmon energy, black trend-line in **Figure 1a**(inset). Therefore, the plasmon's redshift can be directly related to the thermal lattice expansion if an approximation for fixed momentum, strain, and thickness across the membrane holds true. The inset also features two types of error bars (1) capped and (2) shaded. The capped error bars were calculated using a reduced χ^2 analysis of the averaged data points' deviation from a linear fit, normalized to the degrees of freedom. The shaded error bars are the standard deviation of the plasmon energy calculated across all the pixels in the STEM-EELS image at each temperature. This large deviation (average standard deviation in each image ~ 18 meV) is due to imperfect correction of the electron beam angle as it scans across the relatively low magnification image, which results in changes to the beam alignment on the spectrometer's entrance aperture. We expect the experimental uncertainty would improve with higher magnification.

STEM-EELS imaging (**Figure 1b,c**) was performed on an electron-transparent region of the Si with a defect alignment hole shown in the high-angle annular dark-field (HAADF) image survey outside of the STEM-EELS acquisition window. The HAADF image clearly shows the membrane's curvature as bend contours in the image that change with temperature (Supplementary GIFs). The 16x16 pixel STEM-EELS image in **Figure 1c** was collected with the sample at $T_{\text{ref}} = 350$ K. The plasmon energy was determined for each pixel where the zero-loss peak (ZLP) and plasmon peak were center-of-mass fit, and the difference between the two peaks was calculated (see Supplementary Information).

During the STEM-EELS mapping, dualEELS spectral acquisition allowed for sequential acquisition of the ZLP, plasmon, multiple scattering, and Si $L_{2,3}$ edge (**Figure 1d**). Collecting the ZLP through dualEELS is highly critical for core-loss thermometry as it allows for longer acquisitions of the low-intensity core-loss spectrum while still offering a method for spectral alignment. All peak positions were again fit using center-of-mass fitting with careful selection of the fitting window's width and central energy (see Supplementary Information). The spectral redshift with temperature is apparent in the experimental and calculated plasmon and $L_{2,3}$ edge spectra (insets in **Figure 1d,e**).

The average EEL spectrum within each 16x16 pixel STEM-EELS temperature-dependent spectrum image is shown in **Figure 1d**. The direct bandgap ($E_{g,\text{direct}}$), Si main plasmon, and Si $L_{2,3}$ edge are highlighted with insets showing the magnified spectrum. The Si surface plasmon around 10 eV is ignored, as well as the SiO_2 plasmon that is not resolvable at this thickness. Temperature-

dependent spectra in **Figure 1e** were modeled using TDDFT for the ~ 16.8 eV volume plasmon (turboEELS) and DFT/BSE for the ~ 99 eV Si $L_{2,3}$ edge (OCEAN). Thermal lattice expansion was modeled using lattice parameters spanning $a/a_0 = 1.000 - 1.002$ according to the temperature-dependent thermal expansion coefficient and band gap. The lattice parameter was the only input parameter modified across simulations, and the band gap was corrected after the calculation to account for the well-known band gap underestimation using DFT.²⁴ The reference lattice parameter ($a_0 = 10.33$ Bohr) was selected by minimizing the total cell energy.

The *ab initio* TDDFT calculations match the analytical approach for PEET as shown by **Figure 1e**. For PEET on Si, *ab initio* calculations are generally not needed as the thermal lattice expansion is well-studied.⁶ However, more complex materials like transition metal oxides and multi-material stacks/interfaces that contain multiple plasmon and low-loss features are challenging to deconvolute. Instead, an *ab initio* TDDFT approach like the one used here would have to be applied.⁷ Core-loss thermometry is therefore motivated because its element-specificity leads to well-separated spectral features in complex materials. However, first, we must prove that a simple analytical procedure can sufficiently predict the temperature-dependent core-loss spectra without relying on an *ab initio* approach.

Conceptually, the interpretation of temperature-dependent core-level spectra is complicated by complex dependencies of the material's band gap, band curvature, and dielectric function on thermal lattice expansion, lattice vibrational modes, and strain; thus, the mechanism for the previously reported redshift of core-level spectra with temperature remains unclear.^{19,20} To help discern the origin of the redshift, we measure the temperature-dependent differential spectra and compare these results to calculated spectra using the DFT/BSE approach (**Figure 2**). The core-loss spectra were aligned for each STEM-EELS pixel using the low-loss and core-loss Si plasmon peak (the second Si plasmon from multiple scattering) and averaged across each STEM-EELS map. The differential spectra were calculated by first normalizing each core-loss spectrum to span zero to one for the core-loss near edge's minimum and maximum. The spectrum at $T_{\text{ref}} = 75^\circ\text{C} = 350$ K was then subtracted from the corresponding spectrum at each elevated temperature and multiplied by 1000 for visualization (**Figure 2a**). The differential spectra for the DFT/BSE-calculated spectra were similarly obtained (**Figure 2b**).

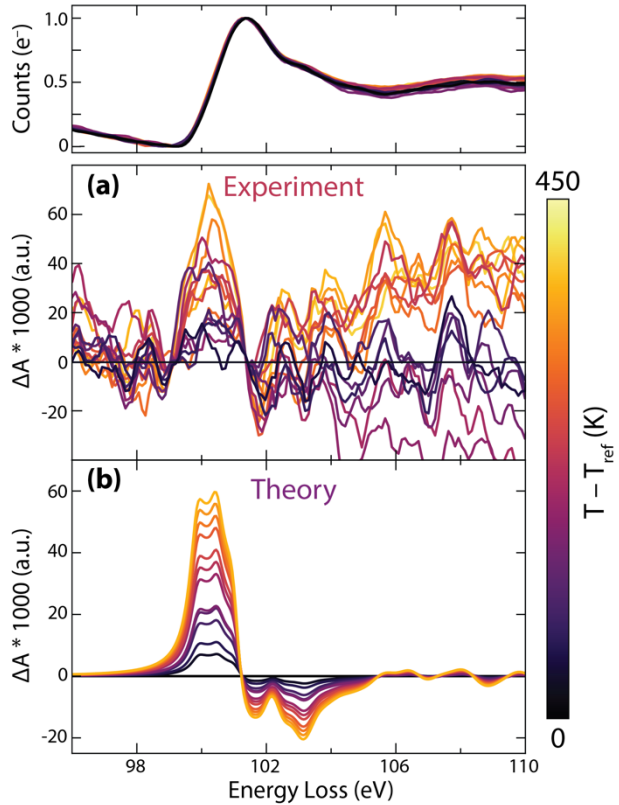


Figure 2. Si $L_{2,3}$ core-loss differential EEL spectra. Measured (a) and modeled (b) differential spectra of the Si $L_{2,3}$ edge from Figure 1d,e. The measured differential is smoothed by a Savitsky-Golay filter (window = 11, order = 3). Only the up-temperature-ramped dataset is plotted. Modeled spectra were calculated using *ab initio* DFT / BSE theory with a scissor shift applied depending on the temperature-dependent band gap [ref. 21].

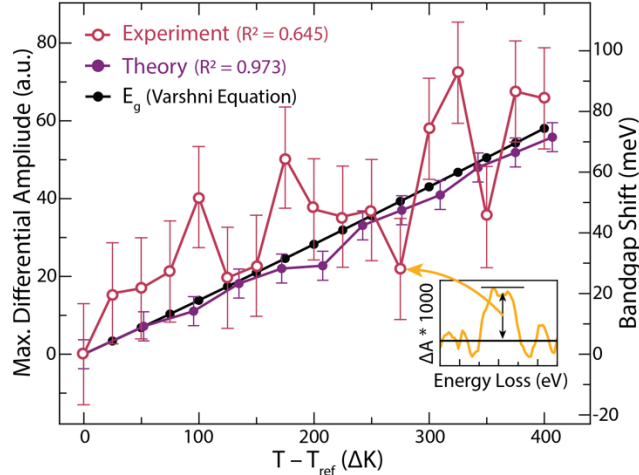


Figure 3. Comparing the modeled and measured Si L_{2,3} edge’s differential amplitude and redshift. The maximum amplitude of the measured (magenta open circles) and modeled (purple filled circles) core-loss differential spectra from Figure 2 is calculated and converted to band gap shift as a function of temperature. The temperature-dependent band gap of Si according to the Varshni equation is shown for reference (black filled circles). $T_{\text{ref}} = 350$ K. The inset shows an example differential spectrum where the amplitude was selected.

the temperature-dependent band gap shift between experiment and theory (**Figure 3**). To convert the differential intensity into the energy of the edge’s redshift, a rigid shift of the T_{ref} spectrum is performed (5 meV shift steps up to 150 meV), and linear regression is used to convert the differential intensity into the meV of the redshift. Both the measured and calculated core-loss spectra are found to follow the Varshni equation. A Varshni equation is an empirical formula that predicts a semiconductor’s band gap (E_g) as a function of temperature (T).^{21,22} A Varshni equation typically has the form $E_g = E_0 - (a * T^2) / (T + b)$ where a and b are derived constants and E_0 is the band gap at 0 K. Whether experimentally measured or computationally derived, an accurate Varshni equation will take into consideration both the thermal lattice expansion and lattice vibrations from electron-phonon renormalization. For covalently bonded materials like Si, the electron-phonon vibrational term dominates because the lattice only minimally expands.

Figure 3 suggests that it is possible to use the core-loss redshift magnitude to determine the Si lattice temperature according to the Varshni equation. Similarly, core-loss thermometry could enable a new approach to directly determine the constants in the Varshni equation for various materials with sub-nm resolution. By determining the constants for bulk specimens using simpler methods (e.g., quantifying the bandgap with UV-Vis spectroscopy) core-loss thermometry could then be used to interrogate more compositionally complex materials and without the need for DFT/BSE calculations. Further, the Varshni equation’s empirical constants could even be derived directly from the temperature-dependent core-loss data.

Figure 4 compares the difference images for $\Delta T = 400$ K. A dark-field difference image (**Figure 4a**) shows changes in the bend contours and membrane curvature at the two temperatures. Dark contrast features show the bend contour positions from the image at T_{ref} , while bright features show their positions at $\Delta T = 400$ K. In the STEM-EELS scanning region indicated by the white-dashed box, PEET and core-loss thermometry is performed.

The differential spectra in **Figure 2** have positive features at the edge onset, indicating the redshift of the core-loss spectra with temperature and lattice expansion as apparent in the **Figure 1d,e** insets. The positive differential feature is almost identical to a rigid spectral shift (**Figure S8**), which suggests the conduction band’s unoccupied density of states is minimally modified at the measured temperatures. X-ray studies often normalize to an intensity far past the edge onset, but multiple scattering in EELS prevented this normalization method.²⁵ Prior to normalization, the near edge intensity decrease produces noise beyond the edge (>102 eV). The DFT/BSE approach used here is also optimized for near-edge features instead of post-edge features. Otherwise, besides experimental noise, the experiment and theory differential spectra are nearly identical.

The maximum differential intensity is calculated to graph the relationship between

PEET imaging is performed by calculating the difference in the plasmon energy between T_{ref} and $\Delta T = 400$ K, and the plasmon energy difference is converted to temperature using linear regression from **Figure 1a**, inset. Core-loss thermometry imaging was similarly performed but analyzed each pixel's Si $L_{2,3}$ edge differential intensity as in **Figure 2**, using a linear regression from **Figure 3**. The PEET and core-loss thermometry images' averages are, respectively, 399 K and 402 K compared to the 400 K set point. The standard deviation across the two thermal images is also ± 201 and ± 1018 K, respectively, while still including statistical outliers. This relatively high variance may be a result of either the scan poor plasmon fitting and alignment to calibrate the energy of the core-loss spectrum.

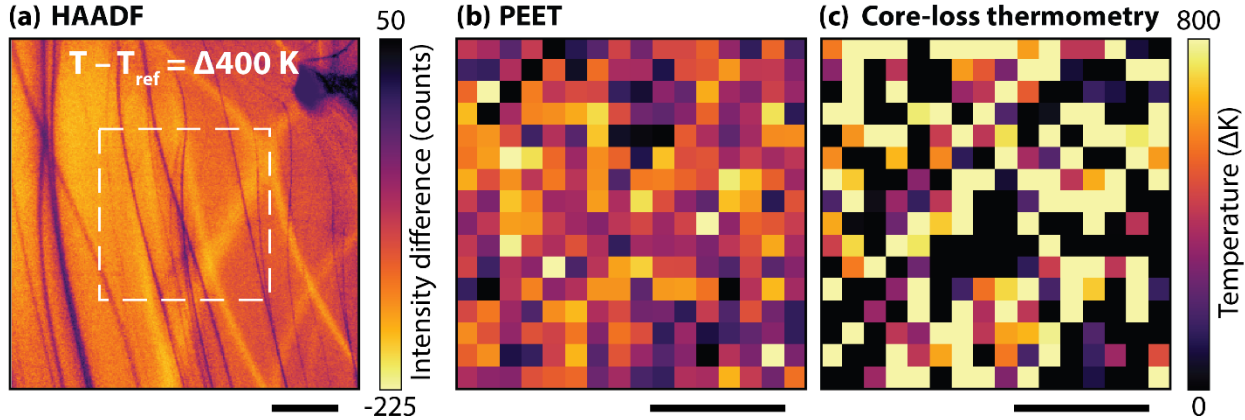


Figure 4. Comparing the Accuracy of Spatially Resolved Plasmon Energy Expansion and Core-Loss Thermometry. (a) A dark-field survey difference image of the Si membrane for a set $\Delta T = 400$ K. STEM-EELS was performed in the white square. (b) A plasmon energy expansion thermometry (PEET) map of the Si membrane for a set $\Delta T = 400$ K. The Si plasmon energy was calculated for each pixel in the original 400 K and T_{ref} images, and each pixel's plasmon energy difference between 400 K and T_{ref} was converted to a measured temperature using linear regression from Figure 1a(inset). (c) A core-loss thermometry map of the Si membrane for a set $\Delta T = 400$ K. The core-loss spectrum at each pixel was aligned using the second Si plasmon, and a differential spectrum was calculated for each pixel. The amplitude of the differential peak resulting from bandgap reduction was converted to temperature using linear regression from Figure 3. Pixels outside two standard deviations were set as the mean at $\Delta 400$ K for visualization only. All scale bars are 5 μm .

DISCUSSION

A comparison of PEET's and core-loss thermometry's ability to extract the thermal expansion coefficient is shown in **Figure 5** and summarized by Table 1. To convert plasmon shift into lattice expansion, we rewrite the free electron model in Equation 1 as: $a(T) / a(T_{\text{ref}}) = (E_p(T) / E_p(T_{\text{ref}}))^{1/3}$. This relationship derives the relative plasmon energy and lattice change, where a is the lattice parameter and the cubed root converts volume into linear space, assuming isotropic expansion. To convert the core-loss red shifted bandgap into the lattice change, we use the reported Varshni equation for Si.²¹ Both the TDDFT and DFT/BSE lattice change for the respective low- and core-loss datasets accurately match the experimentally measured lattice changes.

PEET significantly miscalculates the thermal expansion coefficient (1.79 K^{-1}) by roughly 50% of the expected value reported in literature. This discrepancy could be from the assumption

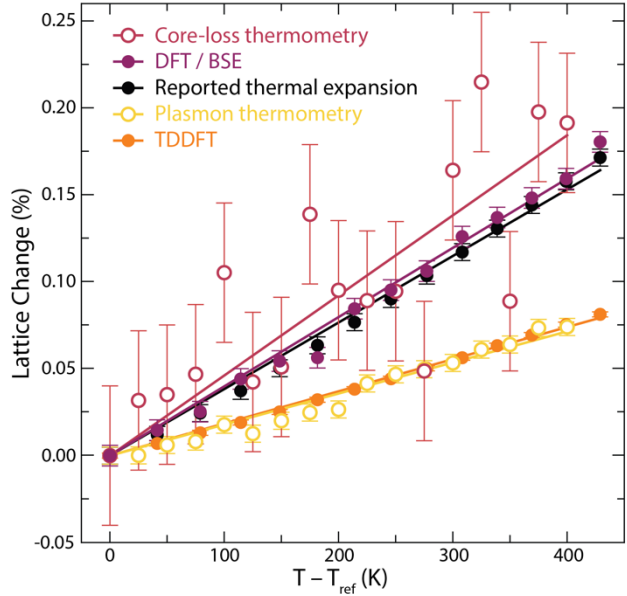


Figure 5. Thermal lattice expansion quantified using low- and core-loss EELS. Four methods of quantifying lattice expansion with temperature are compared to the reported thermal expansion of crystalline Si [ref. 23]. Core-loss thermometry uses the Si $L_{2,3}$ edge shift from the temperature-dependent band gap. Plasmon thermometry uses the plasmon shift following the free electron model. DFT/BSE (core-loss spectra) and TDDFT (plasmon spectra) calculations were performed by isotropically expanding the crystalline Si unit cell, and the DFT/BSE spectra were corrected for the Si bandgap. The slope corresponds to the thermal expansion coefficient (Table 1). The y-intercept is fixed at 0%, and error bars are derived using reduced χ^2 analysis with the plotted linear trend lines.

because image averaging smoothed the edge. It was apparent that most core-loss spectral noise

Table 1. Thermal lattice expansion calculation methods in this work. All measurements were performed on crystalline Si with native oxide. The reported temperature-dependent thermal expansion coefficient (TEC) of Si was used for all inputs [ref. 23], and its fit error results from nonlinearity in this temperature range ($T = 350 - 750$ K).

| Thermal Expansion Measurement | Method | Required Inputs | TEC $\times 10^{-6}$ [K $^{-1}$] | Fit Error*100 (R 2) [unitless] |
|-------------------------------------|----------------|---|-----------------------------------|------------------------------------|
| Reported thermal expansion [ref xx] | — | — | 3.83 | 0.49 (0.996) |
| Plasmon thermometry | Low-loss EELS | Free electron model (ϵ_{∞} , m_{eff}) | 1.79 | 0.49 (0.963) |
| Plasmon thermometry | TDDFT | Free electron model (ϵ_{∞} , m_{eff}), TEC | 1.85 | 0.14 (0.997) |
| Core-loss thermometry | Core-loss EELS | Varshni equation*, TEC | 4.61 | 4.01 (0.615) |
| Core-loss thermometry | DFT/BSE | Varshni equation*, TEC | 3.98 | 0.59 (0.989) |

*The Varshni equation's constants can be taken from literature or derived using the core-loss spectral shift

of constant effective valence band effective mass and dielectric constant with temperature. However, while the effective mass changes by $\sim 5-10\%$ over this temperature range, the dielectric constant would have to change by about 90% to account for the remaining discrepancy.^{26,27} Meanwhile, core-loss thermometry provides a more accurate measure of the thermal lattice expansion (4.61 K^{-1}) but contains larger uncertainty due to the technique's signal-to-noise limitations. This is apparent as the core-loss thermometry data in **Figure 3** has significantly more noise than the plasmon loss data in **Figure 1**. **Table 1** justifies that core-loss thermometry surpasses PEET measurements of thermal expansion coefficients.

Core-loss thermometry, therefore, shows promise for imaging lattice temperatures and the temperature-dependent bandgap at nanometer scales. However, further optimization of the spectral alignment at each pixel is needed to improve the core-loss differential spectrum's signal-to-noise and accuracy, which is even more essential at decreasing length scales. The STEM-EELS images notably required additional Savitzky-Golay smoothing to match the differential amplitude of the image-averaged differential

resulted from plasmon peak misalignment when using the center-of-mass fitting. To improve the plasmon peak alignment, future studies could incorporate residual analysis techniques where the aligned plasmon's residual across low- and core-loss datasets is minimized. Optimizing the acquisition parameters and the signal-to-noise for the core-loss spectra remains critical to improving the accuracy of core-loss thermometry. Balancing the beam current and the detector's live time and total view time will be important to approach sub-nm spatial resolutions without inducing beam damage.

Regarding the observed variations in sample temperature across both the PEET and core-loss thermometry images, the most likely source of uncertainty is the microscope's improper correction of the beam angle at each pixels across the STEM image. This may result in beam alignment inconsistencies onto the spectrometer's entrance aperture, an uncertainty that would be amplified for core-loss imaging (the 99 eV electron scattering angle is greater than that at 16.8 eV). Notably, the variable beam alignment could be minimized at high magnifications. This work utilizes low-magnification STEM to reduce the effects of sample drift with temperature, and we utilize a large defect hole (**Figure 1b**) for image alignment. Low magnification further minimizes beam damage and beam-induced heating. Future studies can avoid sample drift at high magnifications by using high-stability MEMS *in situ* heating holders. Furthermore, plasmon peak alignment error did result in pixel-dependent variations across the core-loss thermometry image (**Figure 4c**), and the plasmon peak alignment could be avoided by using long acquisitions without dualEELS and a spectrometer with high dispersion and stability. Scan-induced momentum effects could appear as localized variance at pixels near the edge of the scanning area, but these momentum-induced effects were not observed. There were no noticeable correlations in any of the datasets when using Pearson and Spearman correlations with p-value testing (see Supplementary Information). Correlations between the dark-field, PEET, core-loss thermometry, and thickness images across the 16x16 pixel scan area were tested.

Sample heating when using a high electron beam current poses further challenges for accurate core-loss thermometry. A microscope's beam current will typically be increased to provide adequate signal-to-noise resolutions of core-loss edges, especially those beyond 1 keV. In this work, the beam current and density used was around 100 pA = 156 pA/ μm^2 and decreased throughout the data acquisition by ~30% due to the cold FEG emission. According to prior PEET literature, 200 kV * 100 pA = 20 mW where roughly 75% of the electrons lose energy to the sample (15 mW) at ~16.8 eV/e⁻.⁶ Therefore, the beam input is 15 mW * (16.8 eV / 200 keV) = <1.3 μW over the 0.64 μm^2 STEM-EELS pixel area. Considering the 1 W/K*m thermal barrier of the 5 nm thick Si oxide, the beam-induced thermal shift would be ~0.01 K per pixel, far below both techniques' resolution limits. However, a careful balance of beam current and dwell time will be essential for mitigating beam-induced artifacts while still acquiring the signal-to-noise needed for core-loss thermometry at sub-nm length scales.

Another concern is that the native SiO₂ oxide layer could introduce local variations in the thermal expansion, potentially affecting the core-loss edge positions due to phase transitions or chemical shifts under prolonged exposure. Fortunately, the ~10 nm total oxide layer plays a less significant role in the spectral response of the ~180 nm Si membrane. The larger effect of the Si oxide is on the membrane's temperature-dependent curvature. Future studies should carefully control the oxide layer and avoid substrates and interfaces that may introduce deleterious temperature-dependent strain or beam heating. Nonetheless, the inherent oxide layer in this work did not significantly influence the STEM-EELS area-averaged measurements as both the core-loss thermometry and PEET followed expected trends. Future studies should investigate the

temperature-dependent strain and momentum effects on the accuracy of PEET and core-loss thermometry.²⁸

In this study, we advance toward a core-loss thermometry approach to map lattice temperatures at the nanoscale, avoiding potential complexities and limitations of PEET. Through a combination of *in situ* STEM-EELS measurements and theoretical modeling, we investigate the origin of temperature-dependent redshifts in low- and core-loss EEL spectra of Si, uncovering why the Si L_{2,3} edge redshifts with temperature. Our findings reveal that the redshift corresponds to the changing bandgap of Si, a phenomenon caused by a combination of thermal lattice expansion and electron-phonon renormalization. The energy of the redshift quantitatively aligns with that predicted by the Varshni equation for Si. Thus, these results highlight the potential of core-loss thermometry to map lattice temperatures and define constants for the Varshni equation in materials with sub-nm spatial resolution and elemental specificity. The results similarly highlight that core-loss EELS, despite its complexity, has a simple interpretation that can be done without *ab initio* calculations, opening its usage to a larger community. Compared to PEET, core-loss thermometry provides a viable alternative for measuring local temperatures in materials with low thermal expansion coefficients or with variable thickness or strain. While signal-to-noise constraints currently limit the spatial resolution of core-loss thermometry, further optimization could enable element-specific temperature mapping at the nanoscale, even during ultrafast and operando measurements. Core-loss thermometry, therefore, offers a promising path to high-resolution, quantitative thermal analysis in an even more diverse class of materials. We foresee great potential for core-loss investigations of thermal strain in multi-element junctions and heat transfer at nanoscale interfaces for microelectronics, photonics, and photocatalytic devices.

METHODS

Temperature-dependent STEM-EELS

All TEM measurements were performed on a JEOL NeoARM microscope with a cold field-emission gun (zero-loss peak FWHM = 0.6 eV). STEM-EELS data was acquired at 200 kV in 8kx low-magnification STEM mode using a 150 cm camera length. The sample was only minimally tilted by 3° in alpha to be off-zone axis, and the tilt angle was not controlled during the thermal sweep. The beam current was approximately 100 pA = 156 pA/μm². The Gatan Continuum Imaging Filter was aligned using a 2.5 mm entrance aperture with 90 meV/ch dispersion and a K3 detector. The Gatan sub-scan feature was enabled to diffuse the beam over the scanning region on the sample and minimize beam-induced heating. The acquisition time was fixed at a 0.5 s view time in dualEELS (1% live time low-loss with 0 eV shift, 50% live time core-loss with 39 eV shift).

A Gatan 652 model heating holder was used for all temperature-dependent STEM-EELS measurements. The sample was first loaded into a vacuum pumping station and heated to 450 °C for 30 minutes to remove surface contamination and then kept under vacuum for ~1 week before the dataset was collected. During STEM-EELS measurements, the holder temperature was first set to 75 °C and the temperature was ramped up in 25 °C steps to 475 °C and then slowly ramped down to check for heating hysteresis. The Si membrane was prepared by mechanical polishing and then ion milling with a PIPS II system.

All STEM-EELS data was analyzed using the hyperspy python loader.²⁹ Center-of-mass fitting was used for all peak fitting (ZLP, Si first plasmon, Si second plasmon) as detailed in the Supplementary Information. Detailed analysis scripts can be provided upon request.

Ab Initio Theory

Density Functional Theory (DFT) Parameters. A 200 Ry cutoff energy was used for all DFT calculations based on convergence tests with a 10.33 Bohr lattice parameter (see test results in Supplementary Information). All DFT self-consistent field calculations utilize a 1×10^{-10} Ry convergence threshold, $16 \times 16 \times 16$ k -point mesh, 6 electronic states (bands), and standard atomic positions for crystalline Si in the diamond cubic crystal structure (fcc lattice with a two-atom basis). The silicon pseudopotential file for all calculations was produced using the ONCVSP code.³⁰ This norm-conserving pseudo was calculated using a PBE functional and nonlinear core correction.

Low-Loss EELS Theory. turboEELS was used to simulate the Si volume plasmon, a program integrated within the Quantum ESPRESSO package.^{31,32} turboEELS calculates the low-loss volume plasmon spectra using a Liouville–Lanczos approach to linearized time-dependent DFT (TDDFT). By calculating the charge-density susceptibility with the quantum Liouville equation, the inverse of the imaginary/longitudinal component of the dielectric function (the EEL spectrum) is simulated. EEL spectra were calculated using DFT and BSE theory.

Core-Loss EELS Theory. To simulate the Si $L_{2,3}$ edge core-loss spectrum, we leverage the Obtaining Core Excitations from the *Ab initio* electronic structure and the NIST BSE solver (OCEAN) package.³³ The OCEAN workflow uses Quantum ESPRESSO to perform DFT calculations of silicon’s electronic structure and subsequently calculates the core-hole exciton effects and core-level spectrum through BSE calculations. OCEAN 3.0.1 and Quantum ESPRESSO 7.0 were used for all calculations. Due to DFT’s well-known inaccuracy in calculating the band gap of materials, a scissor shift corresponding to the temperature-dependent band gap is incorporated for each lattice parameter simulated. The BSE and non-self-consistent field and screening calculations simulate 100 electronic states (bands). The static dielectric constant is fixed to $\epsilon = 11.4$.³⁴

REFERENCES

- (1) Shafique, M.; Garg, S.; Henkel, J.; Marculescu, D. The EDA Challenges in the Dark Silicon Era: Temperature, Reliability, and Variability Perspectives. In *Proceedings of the 51st Annual Design Automation Conference; DAC '14; Association for Computing Machinery: New York, NY, USA, 2014; pp 1–6. https://doi.org/10.1145/2593069.2593229.*
- (2) Ibrahim, A.; Salem, M.; Kamarol, M.; Delgado, M. T.; Desa, M. K. M. Review of Active Thermal Control for Power Electronics: Potentials, Limitations, and Future Trends. *IEEE Open Journal of Power Electronics* **2024**, *5*, 414–435. [https://doi.org/10.1109/OJPEL.2024.3376086.](https://doi.org/10.1109/OJPEL.2024.3376086)
- (3) Zhou, P.; Navid, I. A.; Ma, Y.; Xiao, Y.; Wang, P.; Ye, Z.; Zhou, B.; Sun, K.; Mi, Z. Solar-to-Hydrogen Efficiency of More than 9% in Photocatalytic Water Splitting. *Nature* **2023**, *613* (7942), 66–70. [https://doi.org/10.1038/s41586-022-05399-1.](https://doi.org/10.1038/s41586-022-05399-1)
- (4) Kim, H.; Seo, J. W.; Chung, W.; Narejo, G. M.; Koo, S. W.; Han, J. S.; Yang, J.; Kim, J.-Y.; In, S.-I. Thermal Effect on Photoelectrochemical Water Splitting Toward Highly Solar to

- Hydrogen Efficiency. *ChemSusChem* **2023**, *16* (11), e202202017. <https://doi.org/10.1002/cssc.202202017>.
- (5) Mecklenburg, M.; Hubbard, W. A.; White, E. R.; Dhall, R.; Cronin, S. B.; Aloni, S.; Regan, B. C. Nanoscale Temperature Mapping in Operating Microelectronic Devices. *Science* **2015**, *347* (6222), 629–632. <https://doi.org/10.1126/science.aaa2433>.
 - (6) Mecklenburg, M.; Zutter, B.; Regan, B. C. Thermometry of Silicon Nanoparticles. *Phys. Rev. Appl.* **2018**, *9* (1), 014005. <https://doi.org/10.1103/PhysRevApplied.9.014005>.
 - (7) Hu, X.; Yasaei, P.; Jokisaari, J.; Ögüt, S.; Salehi-Khojin, A.; Klie, R. F. Mapping Thermal Expansion Coefficients in Freestanding 2D Materials at the Nanometer Scale. *Phys. Rev. Lett.* **2018**, *120* (5), 055902. <https://doi.org/10.1103/PhysRevLett.120.055902>.
 - (8) Abe, H.; Terauchi, M.; Kuzuo, R.; Tanaka, M. Temperature Dependence of the Volume-Plasmon Energy in Aluminum. *Journal of Electron Microscopy* **1992**, *41* (6), 465–468. <https://doi.org/10.1093/oxfordjournals.jmicro.a050994>.
 - (9) Hubbard, W. A.; Mecklenburg, M.; Lodico, J. J.; Chen, Y.; Ling, X. Y.; Patil, R.; Kessel, W. A.; Flatt, G. J. K.; Chan, H. L.; Vareskic, B.; Bal, G.; Zutter, B.; Regan, B. C. Electron-Transparent Thermoelectric Coolers Demonstrated with Nanoparticle and Condensation Thermometry. *ACS Nano* **2020**, *14* (9), 11510–11517. <https://doi.org/10.1021/acsnano.0c03958>.
 - (10) Shen, L.; Mecklenburg, M.; Dhall, R.; Regan, B. C.; Cronin, S. B. Measuring Nanoscale Thermal Gradients in Suspended MoS₂ with STEM-EELS. *Applied Physics Letters* **2019**, *115* (153108), 1–5. <https://doi.org/10.1063/1.5094443>.
 - (11) Chmielewski, A.; Ricolleau, C.; Alloyeau, D.; Wang, G.; Nelayah, J. Nanoscale Temperature Measurement during Temperature Controlled in Situ TEM Using Al Plasmon Nanothermometry. *Ultramicroscopy* **2020**, *209*, 112881. <https://doi.org/10.1016/j.ultramic.2019.112881>.
 - (12) Yang, Y.-C.; Serafin, L.; Gauquelin, N.; Verbeeck, J.; Jinschek, J. R. Improving the Accuracy of Temperature Measurement on TEM Samples Using Plasmon Energy Expansion Thermometry (PEET): Addressing Sample Thickness Effects. arXiv August 8, 2024. <https://doi.org/10.48550/arXiv.2407.20059>.
 - (13) Manzke, R. Wavevector Dependence of the Volume Plasmon of GaAs and InSb. *J. Phys. C: Solid State Phys.* **1980**, *13* (5), 911. <https://doi.org/10.1088/0022-3719/13/5/021>.
 - (14) *momentum transfer resolved electron energy-loss spectroscopy, q-EELS | Glossary | JEOL Ltd.* momentum transfer resolved electron energy-loss spectroscopy, q-EELS | Glossary | JEOL Ltd. <https://www.jeol.com/> (accessed 2024-11-01).
 - (15) Roth, F.; König, A.; Fink, J.; Büchner, B.; Knupfer, M. Electron Energy-Loss Spectroscopy: A Versatile Tool for the Investigations of Plasmonic Excitations. *Journal of Electron Spectroscopy and Related Phenomena* **2014**, *195*, 85–95. <https://doi.org/10.1016/j.elspec.2014.05.007>.
 - (16) Liao, K.; Shibata, K.; Mizoguchi, T. Nanoscale Investigation of Local Thermal Expansion at SrTiO₃ Grain Boundaries by Electron Energy Loss Spectroscopy. *Nano Lett.* **2021**, *21* (24), 10416–10422. <https://doi.org/10.1021/acs.nanolett.1c03735>.
 - (17) Espinosa, A.; Castro, G. R.; Reguera, J.; Castellano, C.; Castillo, J.; Camarero, J.; Wilhelm, C.; García, M. A.; Muñoz-Noval, Á. Photoactivated Nanoscale Temperature Gradient Detection Using X-Ray Absorption Spectroscopy as a Direct Nanothermometry Method. *Nano Lett.* **2021**, *21* (1), 769–777. <https://doi.org/10.1021/acs.nanolett.0c04477>.

- (18) Rosen, D. J.; Yang, S.; Marino, E.; Jiang, Z.; Murray, C. B. In Situ EXAFS-Based Nanothermometry of Heterodimer Nanocrystals under Induction Heating. *J. Phys. Chem. C* **2022**, *126* (7), 3623–3634. <https://doi.org/10.1021/acs.jpcc.2c00608>.
- (19) Palmer, L. D.; Lee, W.; Dong, C.-L.; Liu, R.-S.; Wu, N.; Cushing, S. K. Determining Quasi-Equilibrium Electron and Hole Distributions of Plasmonic Photocatalysts Using Photomodulated X-Ray Absorption Spectroscopy. *ACS Nano* **2024**, *18* (13), 9344–9353. <https://doi.org/10.1021/acsnano.3c08181>.
- (20) Rossi, T. C.; Dykstra, C. P.; Haddock, T. N.; Wallick, R.; Burke, J. H.; Gentle, C. M.; Doumy, G.; March, A. M.; van der Veen, R. M. Charge Carrier Screening in Photoexcited Epitaxial Semiconductor Nanorods Revealed by Transient X-Ray Absorption Linear Dichroism. *Nano Lett.* **2021**, *21* (22), 9534–9542. <https://doi.org/10.1021/acs.nanolett.1c02865>.
- (21) Zhang, Y.; Wang, Z.; Xi, J.; Yang, J. Temperature-Dependent Band Gaps in Several Semiconductors: From the Role of Electron–Phonon Renormalization. *J. Phys.: Condens. Matter* **2020**, *32* (47), 475503. <https://doi.org/10.1088/1361-648X/aba45d>.
- (22) Ponce, S.; Gillet, Y.; Laflamme Janssen, J.; Marini, A.; Verstraete, M.; Gonze, X. Temperature Dependence of the Electronic Structure of Semiconductors and Insulators. *Journal of Chemical Physics* **2015**, *143* (102813). <https://doi.org/10.1063/1.4927081>.
- (23) Watanabe, H.; Yamada, N.; Okaji, M. Linear Thermal Expansion Coefficient of Silicon from 293 to 1000 K. *International Journal of Thermophysics* **2004**, *25* (1), 221–236. <https://doi.org/10.1023/B:IJOT.0000022336.83719.43>.
- (24) Perdew, J. P. Density Functional Theory and the Band Gap Problem. *International Journal of Quantum Chemistry* **1985**, *28* (S19), 497–523. <https://doi.org/10.1002/qua.560280846>.
- (25) Zoric, M. R.; Basera, P.; Palmer, L. D.; Aitbekova, A.; Powers-Riggs, N.; Lim, H.; Hu, W.; Garcia-Esparza, A. T.; Sarker, H.; Abild-Pedersen, F.; Atwater, H. A.; Cushing, S. K.; Bajdich, M.; Cordones, A. A. Oxidizing Role of Cu Cocatalysts in Unassisted Photocatalytic CO₂ Reduction Using P-GaN/Al₂O₃/Au/Cu Heterostructures. *ACS Nano* **2024**, *18* (30), 19538–19548. <https://doi.org/10.1021/acsnano.4c02088>.
- (26) Lautenschlager, P.; Garriga, M.; Vina, L.; Cardona, M. Temperature Dependence of the Dielectric Function and Interband Critical Points in Silicon. *Phys. Rev. B* **1987**, *36* (9), 4821–4830. <https://doi.org/10.1103/PhysRevB.36.4821>.
- (27) Green, M. Intrinsic Concentration, Effective Densities of States, and Effective Mass in Silicon. *Journal of Applied Physics* **1990**, *67*, 2944–2954.
- (28) Palmer, L. D.; Lee, W.; Gage, T. E.; Cushing, S. K. Mapping Nanoscale Anisotropic Thermal Expansion and Strain through Correlative Diffraction, Imaging, and Spectroscopy in the TEM. *Microscopy and Microanalysis* **2024**, *30* (Supplement_1), ozae044.682. <https://doi.org/10.1093/mam/ozae044.682>.
- (29) Peña, F. de la; Prestat, E.; Fauske, V. T.; Lähnemann, J.; Burdet, P.; Jokubauskas, P.; Furnival, T.; Francis, C.; Nord, M.; Ostasevicius, T.; MacArthur, K. E.; Johnstone, D. N.; Sarahan, M.; Taillon, J.; Aarholt, T.; pquinn-dls; Migunov, V.; Eljarrat, A.; Caron, J.; Nemoto, T.; Poon, T.; Mazzucco, S.; actions-user; Tappy, N.; Cautaerts, N.; Somnath, S.; Slater, T.; Walls, M.; pietsjoh; Ramsden, H. Hyperspy/Hyperspy: V2.1.1, 2024. <https://doi.org/10.5281/zenodo.12724131>.
- (30) Hamann, D. R. Optimized Norm-Conserving Vanderbilt Pseudopotentials. *Phys. Rev. B* **2013**, *88* (8), 085117. <https://doi.org/10.1103/PhysRevB.88.085117>.

- (31) Timrov, I.; Vast, N.; Gebauer, R.; Baroni, S. turboEELS—A Code for the Simulation of the Electron Energy Loss and Inelastic X-Ray Scattering Spectra Using the Liouville–Lanczos Approach to Time-Dependent Density-Functional Perturbation Theory. *Computer Physics Communications* **2015**, *196*, 460–469. <https://doi.org/10.1016/j.cpc.2015.05.021>.
- (32) Giannozzi, P.; Baroni, S.; Bonini, N.; Calandra, M.; Car, R.; Cavazzoni, C.; Ceresoli, D.; Chiarotti, G. L.; Cococcioni, M.; Dabo, I.; Corso, A. D.; Gironcoli, S. de; Fabris, S.; Fratesi, G.; Gebauer, R.; Gerstmann, U.; Gougoussis, C.; Kokalj, A.; Lazzeri, M.; Martin-Samos, L.; Marzari, N.; Mauri, F.; Mazzarello, R.; Paolini, S.; Pasquarello, A.; Paulatto, L.; Sbraccia, C.; Scandolo, S.; Sclauzero, G.; Seitsonen, A. P.; Smogunov, A.; Umari, P.; Wentzcovitch, R. M. QUANTUM ESPRESSO: A Modular and Open-Source Software Project for Quantum Simulations of Materials. *J. Phys.: Condens. Matter* **2009**, *21* (39), 395502. <https://doi.org/10.1088/0953-8984/21/39/395502>.
- (33) Vinson, J. Advances in the OCEAN-3 Spectroscopy Package. *Phys. Chem. Chem. Phys.* **2022**, *24* (21), 12787–12803. <https://doi.org/10.1039/D2CP01030E>.
- (34) Baroni, S.; Resta, R. Ab Initio Calculation of the Macroscopic Dielectric Constant in Silicon. *Phys. Rev. B* **1986**, *33* (10), 7017–7021. <https://doi.org/10.1103/PhysRevB.33.7017>.

ACKNOWLEDGEMENTS

The authors thank Professor Ye-Jin Kim, Professor Oh-Hoon Kwon, Dr. Haihua Liu, Nicholas Heller, and Nicholas Hagopian for helpful research discussions regarding project directions and data analysis. The authors also thank Dr. Jianguo Wen and Dr. Yuzi Liu for contributing to sample preparation and microscope alignment.

This research was supported as part of the Ensembles of Photosynthetic Nanoreactors, an Energy Frontier Research Center funded by the U.S. Department of Energy, Office of Science under Award No. DE-SC0023431. STEM-EELS measurements were performed at the Center for Nanoscale Materials, a U.S. Department of Energy Office of Science User Facility, supported by the U.S. DOE, Office of Basic Energy Sciences, under Contract No. DE-AC02-06CH11357 through User Proposal #82934. The computations presented here were conducted in the Resnick High Performance Computing Center, a Resnick Sustainability Institute facility at the California Institute of Technology.

L.D.P. was supported by the National Science Foundation Graduate Research Fellowship under Grant No. DGE-1745301 and the Office of Science Graduate Student Research (SCGSR) program. The SCGSR program is administered by the Oak Ridge Institute for Science and Education for the U.S. Department of Energy, Office of Science under contract No. DE-SC0014664. W.L. acknowledges support from the Korea Foundation for Advanced Studies.

AUTHOR INFORMATION

Affiliations

¹California Institute of Technology, Division of Chemistry and Chemical Engineering, Pasadena, CA, USA

²Sandia National Laboratories, Livermore, California 94551, USA

³Argonne National Laboratory, Center for Nanoscale Materials, Lemont, IL, USA

Contributions

L.D.P., W.L., T.E.G., and S.K.C. conceptualized and designed the project scope. L.D.P. acquired the data, performed the data analysis, and prepared the manuscript. L.D.P. and W.L. performed the computational modeling. T.E.G. led the microscopy efforts, approach, and alignment. S.K.C supervised the project and its funding. All authors provided feedback and direction during the manuscript submission and review.

Corresponding Author

Correspondence to [Thomas E. Gage](#) & [Scott K. Cushing](#)

SUPPLEMENTARY INFORMATION

Towards Nanoscale and Element-Specific Lattice Temperature Measurements using Core-Loss Electron Energy-Loss Spectroscopy

Levi D. Palmer,¹ Wonseok Lee,¹ Javier Fajardo, Jr.,² A. Alec Talin,² Thomas E. Gage,^{3,*} Scott K. Cushing^{1,*}

¹California Institute of Technology, Division of Chemistry and Chemical Engineering, Pasadena, CA, USA

²Sandia National Laboratories, Livermore, California 94551, USA

³Argonne National Laboratory, Center for Nanoscale Materials, Lemont, IL, USA

*Correspondence to [Thomas E. Gage](#) & [Scott K. Cushing](#)

Table of Contents

| | |
|---|-----------|
| SUPPLEMENTARY INFORMATION | 16 |
| Experimental Data | 17 |
| STEM-EELS Data Analysis | 23 |
| PEET Analysis Script..... | 23 |
| Core-Loss Thermometry Analysis Script..... | 25 |
| Computational Methods | 28 |
| Scissor Shift Applied to OCEAN Data: | 30 |
| Simulated Lattice Parameters (OCEAN and turboEELS): | 30 |
| Example turboEELS Input File:..... | 31 |
| Example OCEAN Input File: | 33 |

Experimental Data

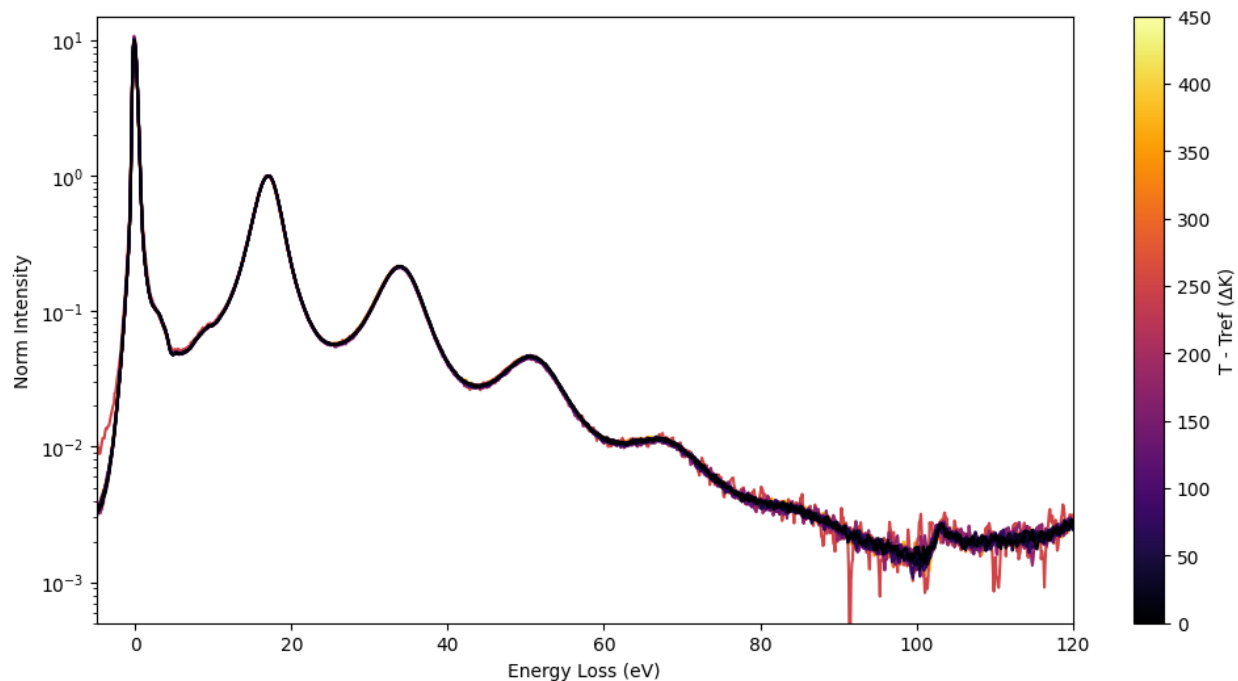


Figure S1. The entire EEL spectrum in log scale. All low-energy spectra are plotted together in log scale without the dualEELS core-loss (high-loss) spectra displayed. By using longer acquisition times and without spectral drift, the core-loss Si $L_{2,3}$ edge would be resolvable at the dispersion used.

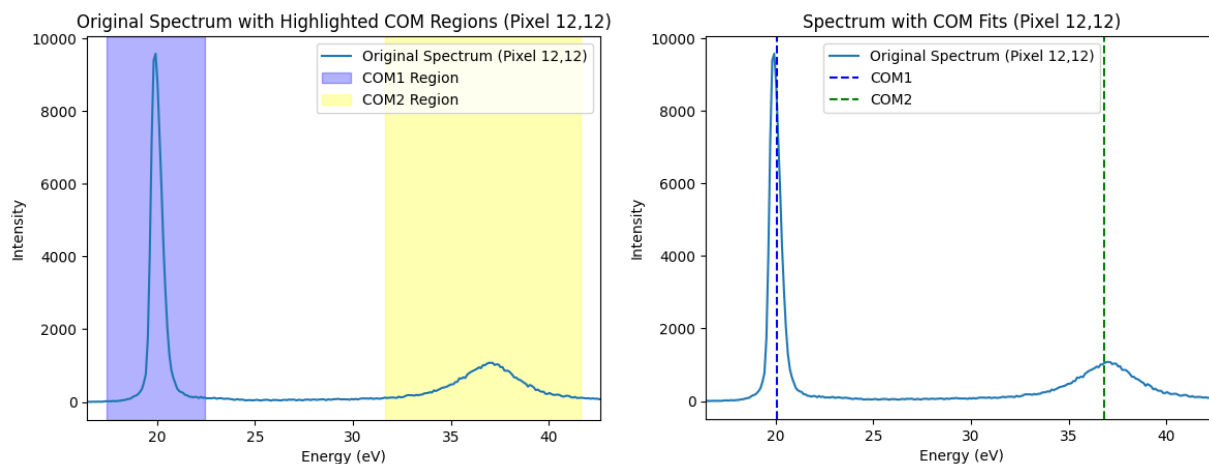


Figure S2. Visual inspection of the center-of-mass fitting windows. The center-of-mass fitting windows for the zero-loss peak and the Si plasmon peak are highlighted in blue and yellow, respectively, in the left image. The resulting center-of-mass fits for this corresponding pixel in the first STEM-EELS image are displayed as dashed vertical lines in the right image.

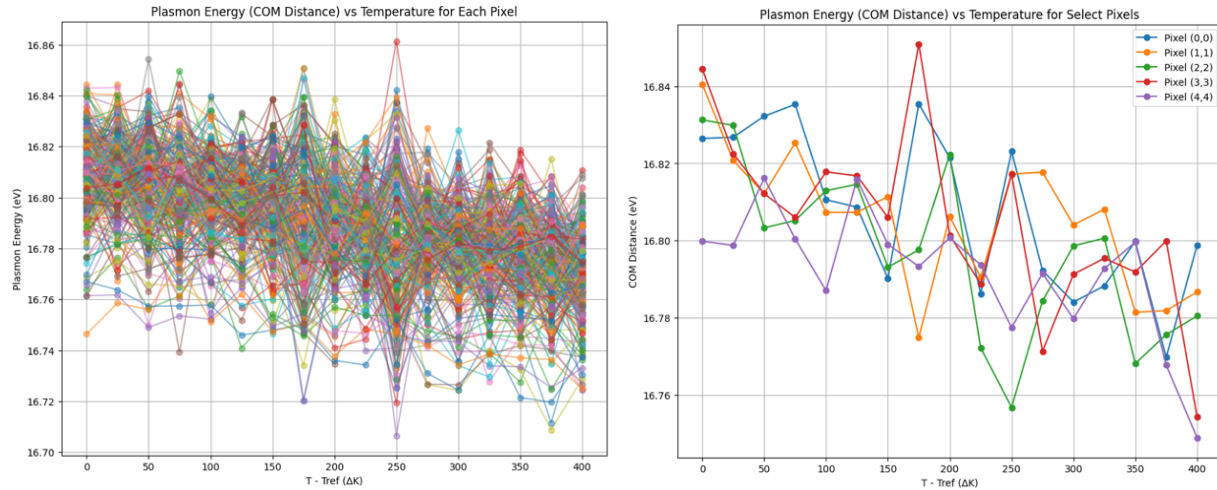


Figure S3. Plasmon energy variations at individual pixels and across temperatures. To compare the effects of the STEM scan’s pixel-dependent beam alignment and the center-of-mass fit accuracy, the plasmon energy at each pixel across all measured temperatures is displayed. The left image displays all pixels (256), and the right image displays only the first five pixels across the image diagonal. It is apparent that the beam deflection and center-of-mass fitting both influence the accuracy of the PEET imaging.

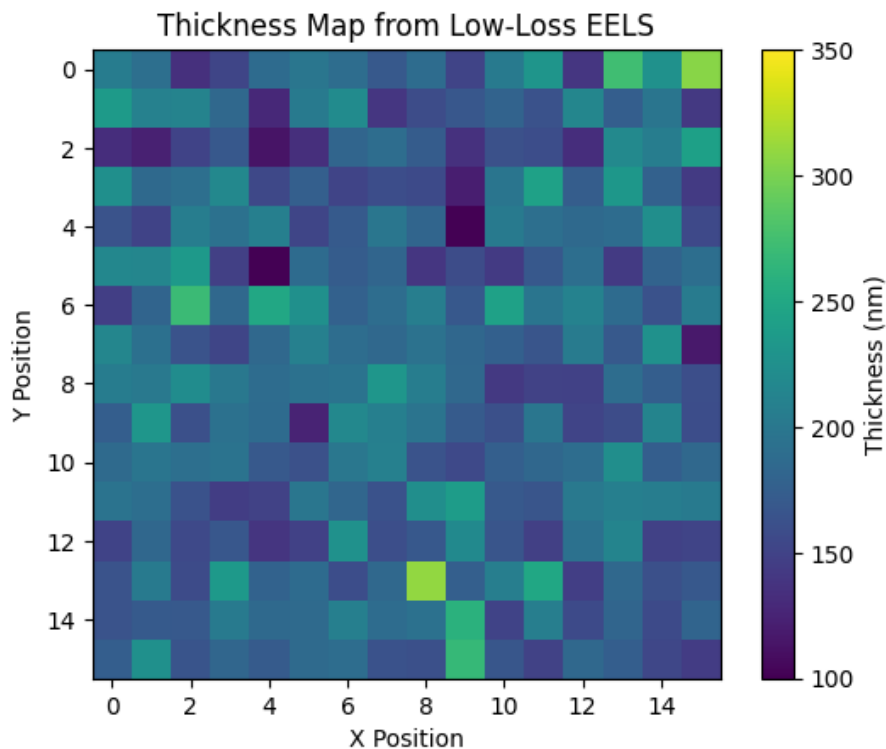


Figure S4. Thickness mapping across the STEM-EELS low-loss image at T_{ref} . The log-ratio method was used to calculate the sample thickness by summing the electron counts over the ZLP (10 eV window) and the plasmon region (75 eV window). Average thickness = 182.6 ± 33.7

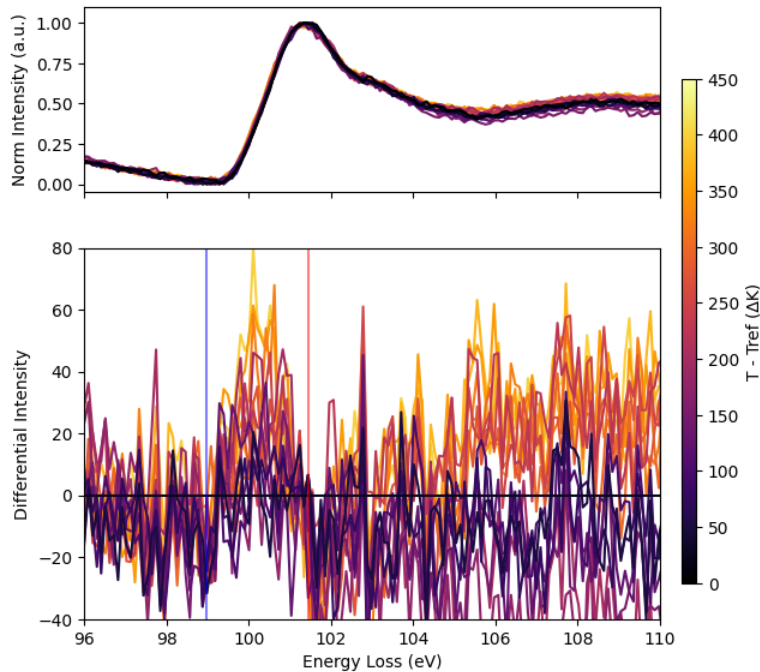


Figure S5. Full Si $L_{2,3}$ differentials without smoothing. To accurately visualize the differential spectra's signal-to-noise, the spectra are displayed without smoothing (used largely for visualization purposes). Each spectrum is the average spectrum across the STEM-EELS image at the temperature indicated by the color axis.

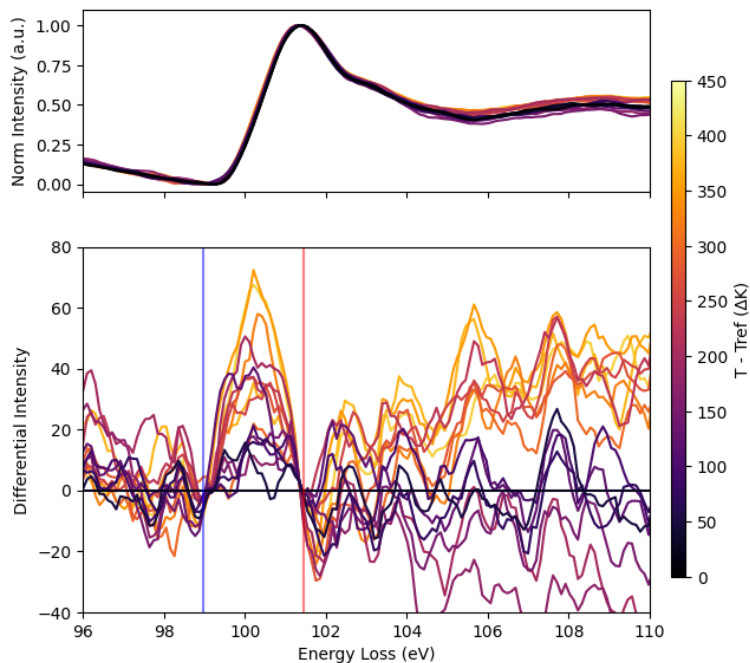


Figure S6. Si $L_{2,3}$ differentials and indicators for spectral normalization window. The core-loss spectra were normalized to the minimum and maximum intensity of the edge plotted above (spanning zero to one in intensity). The normalization areas are indicated by the vertical lines.

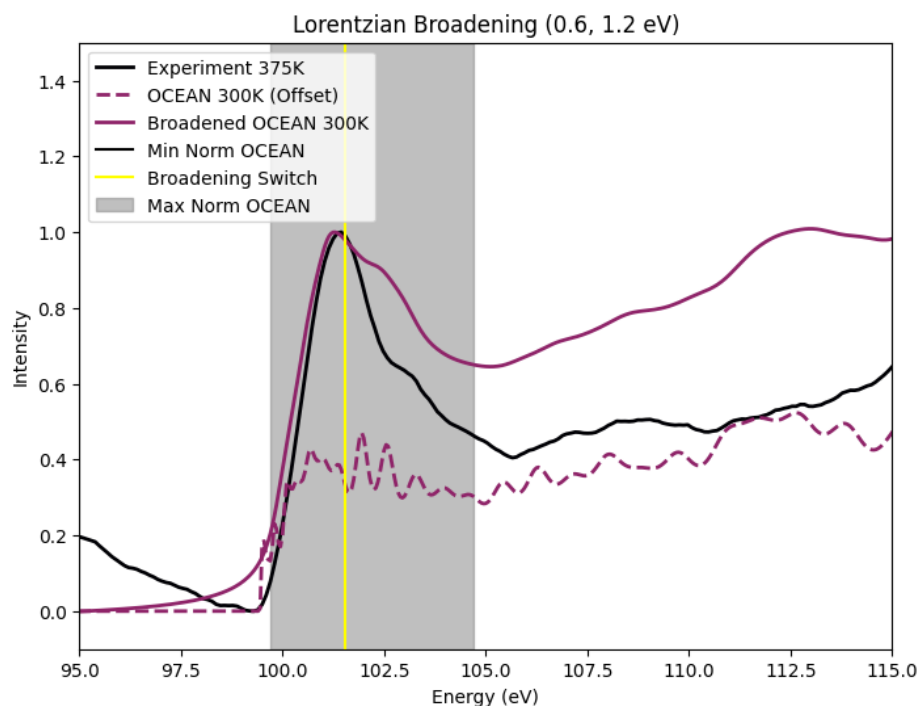


Figure S7. Comparing calculated and experimental Si $L_{2,3}$ spectra. To visualize the effects of energy-dependent Lorentzian broadening, the OCEAN output (before broadening) is displayed offset. The gray shaded region indicates the area used to normalize the OCEAN data, and the yellow vertical line indicates the energy at which more Lorentzian broadening started to be applied (0.6 eV to a maximum of 1.2 eV broadening). More broadening can be applied to improve the match between experiment and theory, but the results may be non-physical.

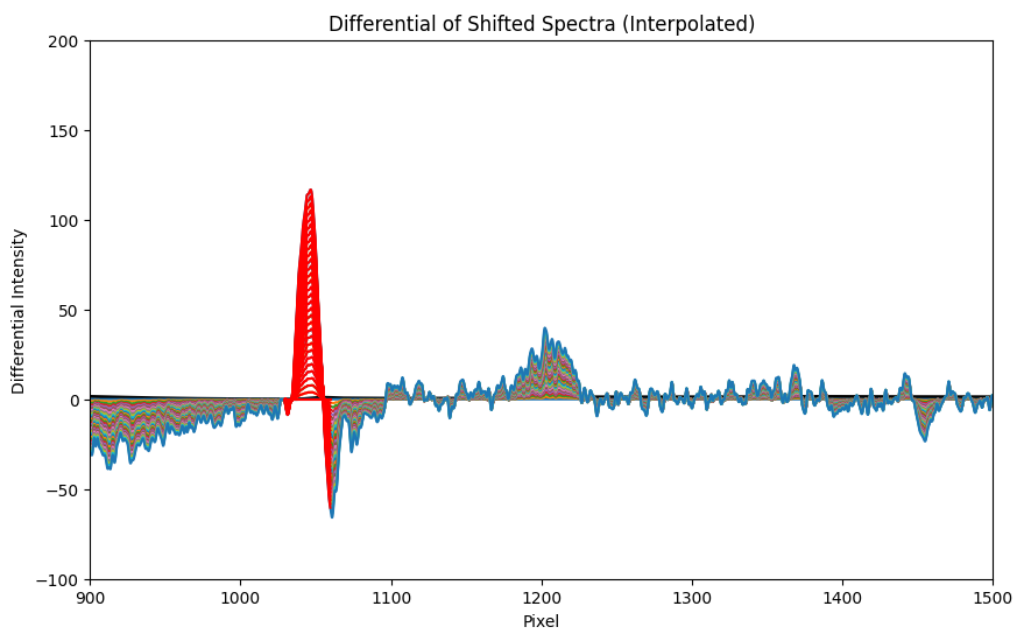


Figure S8. Rigid spectral shift. The rigid-shifted reference spectrum at T_{ref} was shifted in 5 meV increments up to 105 meV. The maximum amplitude of the differential intensity (area analyzed fit in red) was then calculated and used to convert differential amplitude into meV spectral shift.

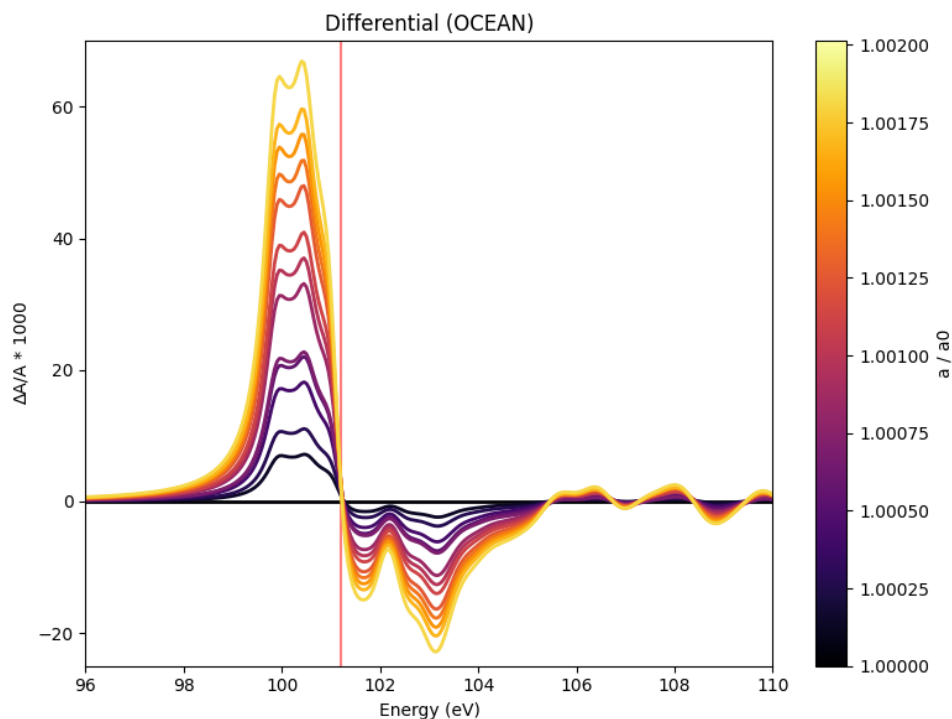


Figure S9. Spectral normalization windows for Si L_{2,3} calculated spectra. The OCEAN-calculated Si L_{2,3} edge is plotted as a function of temperature. The red vertical line depicts the normalization window selected for the spectra after they are shifted as a function of temperature.

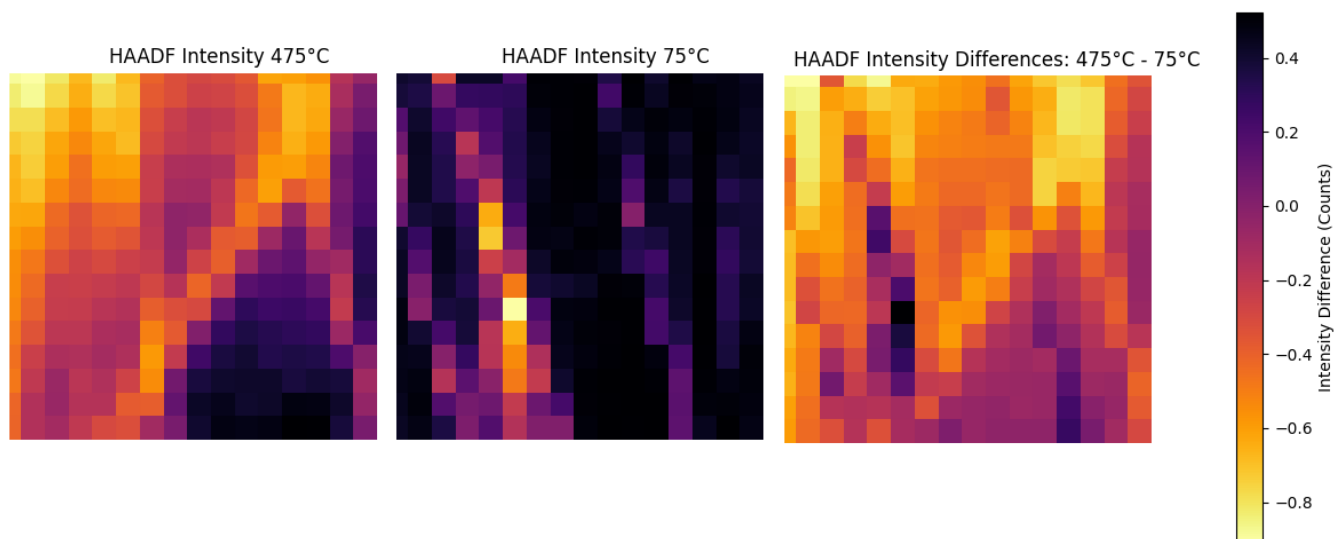


Figure S10. HAADF intensity images. The HAADF intensity at each pixel in the STEM images was also acquired and can be analyzed alongside the STEM-EELS data when looking for correlations in the datasets (see **Figure S11**). The first two HAADF images plotted have normalized intensities spanning 0 (yellow) to 1 (black).

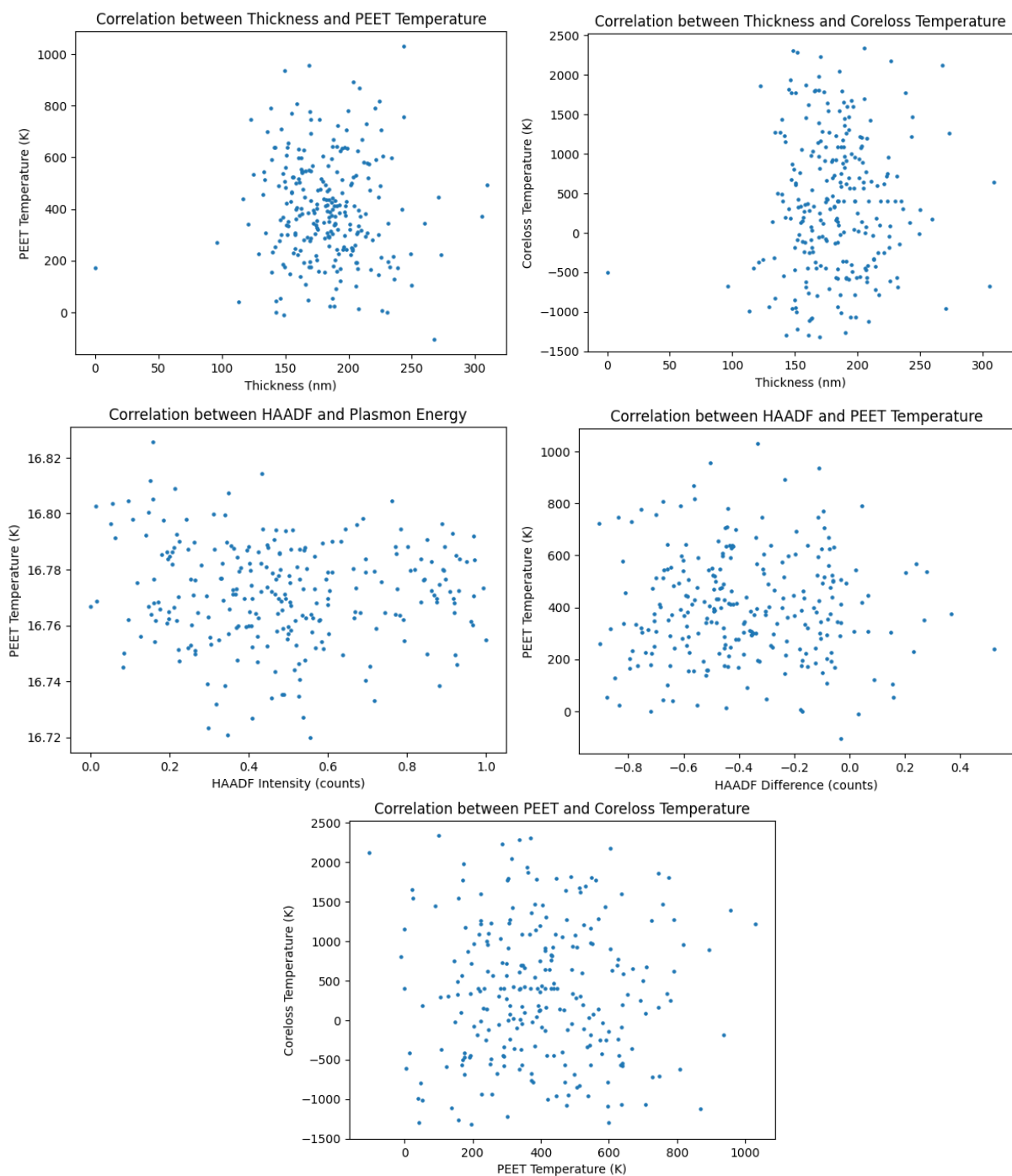


Figure S11. Correlation plots. A Spearman and Pearson correlation algorithm and correlation plot was calculated to determine if there were correlations amongst the datasets. This would potentially indicate pixel-by-pixel errors associated with the datasets and sources of uncertainty. However, no correlations were found. See below for the correlation functions in python:
`pearson_haadf_corr, pearson_haadf_p_value = pearsonr(haadf_flat, temp_peat_flat)`
`spearman_haadf_corr, spearman_haadf_p_value = spearmanr(haadf_flat, temp_peat_flat)`

STEM-EELS Data Analysis

PEET Analysis Script

```
# Calculate Plasmon COM Distances in each STEM-EELS Image Pixel, Generate COM PEET Imaging GIF
```

```
com_distances_all_temps = np.zeros((len(temp_C), image_size[0], image_size[1]))  
avg_com_distances, com_distance_stddevs, avg_spectra_per_temp, frames = [], [], [], []  
vmin_value, vmax_value = 16.75, 16.85  
output_gif_path = directory +'/Figures/Plasmon_ZLP_Distances_Gif.gif'
```

```
# Fit, shift, average, and plot spectra across temperatures
```

```
scale_length = 6 # Length of the scale bar in pixels
```

```
pixel_size = 0.8256 # Pixel size in microns
```

```
scale_bar_um = scale_length * pixel_size # Convert scale length to microns
```

```
for temp_idx, (filename, temp) in enumerate(zip(files_list, temp_C)):
```

```
    file_path = os.path.join(directory, filename)
```

```
    dataset_list = hs.load(file_path)
```

```
    lowloss_signal = dataset_list[2]
```

```
    matrix_size = lowloss_signal.data.shape[:2]
```

```
    energy_axis = np.arange(len(lowloss_signal.data[0, 0])) * pix_scale
```

```
    extended_energy_axis = np.linspace(energy_axis[0] - extra_range, energy_axis[-1] +  
extra_range, len(energy_axis) + 2 * extra_range)
```

```
    com1_values, com2_values, distance_com = np.zeros(matrix_size), np.zeros(matrix_size),  
np.zeros(matrix_size)
```

```
    shifted_spectra = np.zeros((matrix_size[0], matrix_size[1], len(extended_energy_axis)))
```

```
    for i in range(matrix_size[0]):
```

```
        for j in range(matrix_size[1]):
```

```
            lowloss_spectrum_data = lowloss_signal.inav[i, j].data
```

```
            peak_index = np.argmax(lowloss_spectrum_data)
```

```
            com1_start, com1_end = max(peak_index - com1_window // 2, 0), min(peak_index +  
com1_window // 2, len(lowloss_spectrum_data))
```

```
            x_com1_region, y_com1_region = np.arange(com1_start, com1_end),
```

```
lowloss_spectrum_data[com1_start:com1_end]
```

```
            com1 = np.sum(x_com1_region * y_com1_region) / np.sum(y_com1_region) if  
np.sum(y_com1_region) > 0 else 0
```

```
            energy_shift = com1 * pix_scale
```

```
            shifted_spectra[i, j, :] = np.interp(extended_energy_axis, energy_axis - energy_shift,  
lowloss_spectrum_data, left=0, right=0)
```

```
            com2_center = int(com1 + com2_offset_eV / pix_scale)
```

```
            com2_start, com2_end = max(com2_center - com2_window // 2, 0), min(com2_center +  
com2_window // 2, len(lowloss_spectrum_data))
```

```
            x_com2_region, y_com2_region = np.arange(com2_start, com2_end),
```

```
lowloss_spectrum_data[com2_start:com2_end]
```

```
            com2 = np.sum(x_com2_region * y_com2_region) / np.sum(y_com2_region) if  
np.sum(y_com2_region) > 0 else 0
```



```

        com1_values[i, j], com2_values[i, j], distance_com[i, j] = com1, com2, abs(com1 - com2)
* pix_scale

# Save the COM distances for each pixel for this temperature
com_distances_all_temps[temp_idx, :, :] = distance_com

# Append only once per temperature
avg_com_distances.append(np.mean(distance_com))
com_distance_stddevs.append(np.std(distance_com))

# Calculate and append the average spectrum for this temperature
avg_spectrum = np.mean(shifted_spectra, axis=(0, 1)) # Average over the spatial dimensions
(i, j)
avg_spectra_per_temp.append(avg_spectrum)

# Create the main figure and plot area
fig, ax = plt.subplots(figsize=(6, 6))
fig.subplots_adjust(bottom=0.25) # Extra space at the bottom for the scale bar

# Display the main data image
im = ax.imshow(distance_com, cmap='inferno_r', vmin=vmin_value, vmax=vmax_value)
plt.colorbar(im, ax=ax, label='COM Distance (eV)')
ax.axis('off')
ax.text(-0.05, -0.05, f'Tref =  $\Delta$ {temp_Kref[temp_idx]:.2f} K', color='black', fontsize=12,
transform=ax.transAxes)

# Add an inset axis specifically for the scale bar
inset_ax = fig.add_axes([0.5, 0.1, 1, 0.05]) # [left, bottom, width, height] - adjust as needed
inset_ax.axis("off") # Hide inset axis borders and ticks

# Draw the rectangle as a scale bar on the inset axis
rect = Rectangle((0, 0), 1, 0.2, transform=inset_ax.transAxes, linewidth=1,
                edgecolor='black', facecolor='black')
inset_ax.add_patch(rect)
inset_ax.text(0.5, -0.3, f'{scale_bar_um:.1f}  $\mu$ m', ha='center', va='top', color='black',
fontsize=12, transform=inset_ax.transAxes)

# Render the canvas and save each frame
fig.canvas.draw()
frames.append(np.frombuffer(fig.canvas.tostring_rgb(),
dtype='uint8').reshape(fig.canvas.get_width_height()[::-1] + (3,)))
plt.close(fig)

# Save the GIF from collected frames
imageio.mimsave(output_gif_path, frames, fps=2) # Adjust fps as needed

```

Core-Loss Thermometry Analysis Script

```
# Fit all the STEM-EELS core-loss thermometry data

# Define constants
com_ZLP_window = 100 # 75 pixel window around the first peak for ZLP
com_plasmon_window = 150 # 150 pixel window for the plasmon peaks
extra_range = 5 # Extend the energy axis by 5 eV on both sides
plasmon_expected_energy = 33.5 # Approximate energy position of the second plasmon peak

# Initialize arrays to store average shifted spectra for each temperature
avg_shifted_lowloss_per_temp = []
avg_shifted_coreloss_per_temp = []

# Iterate over all temperatures and their respective files
for temp_idx, filename in enumerate(files_list):

    # Load the current file
    file_path = os.path.join(directory, filename)
    dataset_list = hs.load(file_path)

    # Extract low-loss and core-loss signals for the current temperature
    lowloss_signal = dataset_list[2] # Assuming the 3rd dataset is low-loss
    coreloss_signal = dataset_list[3] # Assuming the 4th dataset is core-loss

    # Determine the matrix size dynamically
    matrix_size = lowloss_signal.data.shape[:2]

    # Define the original and extended energy axis
    energy_axis = np.arange(len(lowloss_signal.data[0, 0])) * pix_scale
    extended_energy_axis = np.linspace(energy_axis[0] - extra_range, energy_axis[-1] +
    extra_range, len(energy_axis) + 2 * extra_range)

    # Initialize arrays to hold the shifted spectra for the 2D image
    shifted_lowloss_spectra = np.zeros((matrix_size[0], matrix_size[1],
    len(extended_energy_axis)))
    shifted_coreloss_spectra = np.zeros((matrix_size[0], matrix_size[1],
    len(extended_energy_axis)))

    # Loop through each pixel in the 2D image
    for i in range(matrix_size[0]):
        for j in range(matrix_size[1]):
            # Extract low-loss and core-loss spectra for the current pixel
            lowloss_spectrum_data = lowloss_signal.inav[i, j].data
            coreloss_spectrum_data = coreloss_signal.inav[i, j].data
```

```

# Perform COM fitting for ZLP and plasmon peaks
peak_index_ZLP = np.argmax(lowloss_spectrum_data)
ZLP_start = max(peak_index_ZLP - com_ZLP_window // 2, 0)
ZLP_end = min(peak_index_ZLP + com_ZLP_window // 2, len(lowloss_spectrum_data))
x_ZLP_region = np.arange(ZLP_start, ZLP_end)
y_ZLP_region = lowloss_spectrum_data[ZLP_start:ZLP_end]

if np.sum(y_ZLP_region) > 0:
    com_ZLP = np.sum(x_ZLP_region * y_ZLP_region) / np.sum(y_ZLP_region)
else:
    com_ZLP = 0

# Search for the maximum of the second plasmon peak in a region around 32.8 eV from
the ZLP
plasmon_lowloss_region_start = int(com_ZLP + (plasmon_expected_energy - 5) /
pix_scale)
plasmon_lowloss_region_end = int(com_ZLP + (plasmon_expected_energy + 5) /
pix_scale)
plasmon_lowloss_region =
lowloss_spectrum_data[plasmon_lowloss_region_start:plasmon_lowloss_region_end]

# Find the actual maximum of the plasmon peak in this region
plasmon_lowloss_max_index = np.argmax(plasmon_lowloss_region) +
plasmon_lowloss_region_start

# Center the window around the maximum position of the second plasmon peak
plasmon_lowloss_start = max(plasmon_lowloss_max_index - com_plasmon_window //
2, 0)
plasmon_lowloss_end = min(plasmon_lowloss_max_index + com_plasmon_window // 2,
len(lowloss_spectrum_data))
x_plasmon_lowloss_region = np.arange(plasmon_lowloss_start, plasmon_lowloss_end)
y_plasmon_lowloss_region =
lowloss_spectrum_data[plasmon_lowloss_start:plasmon_lowloss_end]

if np.sum(y_plasmon_lowloss_region) > 0:
    com_plasmon_lowloss = np.sum(x_plasmon_lowloss_region *
y_plasmon_lowloss_region) / np.sum(y_plasmon_lowloss_region)
else:
    com_plasmon_lowloss = 0

# Core-loss plasmon peak fitting
peak_index_plasmon_coreloss = np.argmax(coreloss_spectrum_data)
plasmon_coreloss_start = max(peak_index_plasmon_coreloss - com_plasmon_window //
2, 0)
plasmon_coreloss_end = min(peak_index_plasmon_coreloss + com_plasmon_window //
2, len(coreloss_spectrum_data))

```

```

x_plasmon_coreloss_region = np.arange(plasmon_coreloss_start, plasmon_coreloss_end)
y_plasmon_coreloss_region =
coreloss_spectrum_data[plasmon_coreloss_start:plasmon_coreloss_end]

if np.sum(y_plasmon_coreloss_region) > 0:
    com_plasmon_coreloss = np.sum(x_plasmon_coreloss_region *
y_plasmon_coreloss_region) / np.sum(y_plasmon_coreloss_region)
else:
    com_plasmon_coreloss = 0

# Shift the low-loss spectrum using the ZLP COM
energy_shift_lowloss = com_ZLP * pix_scale
shifted_lowloss_spectra[i, j, :] = np.interp(extended_energy_axis, energy_axis -
energy_shift_lowloss, lowloss_spectrum_data, left=0, right=0)

# Shift the core-loss spectrum such that the plasmon peak aligns with the low-loss
plasmon peak
energy_shift_coreloss = (com_plasmon_coreloss - com_plasmon_lowloss + com_ZLP) *
pix_scale
shifted_coreloss_spectra[i, j, :] = np.interp(extended_energy_axis, energy_axis -
energy_shift_coreloss, coreloss_spectrum_data, left=0, right=0)

# Average the shifted spectra over all pixels for this temperature
avg_shifted_lowloss_spectrum = np.mean(shifted_lowloss_spectra, axis=(0, 1))
avg_shifted_coreloss_spectrum = np.mean(shifted_coreloss_spectra, axis=(0, 1))

# Store the average spectra for this temperature
avg_shifted_lowloss_per_temp.append(avg_shifted_lowloss_spectrum)
avg_shifted_coreloss_per_temp.append(avg_shifted_coreloss_spectrum)

```

Computational Methods

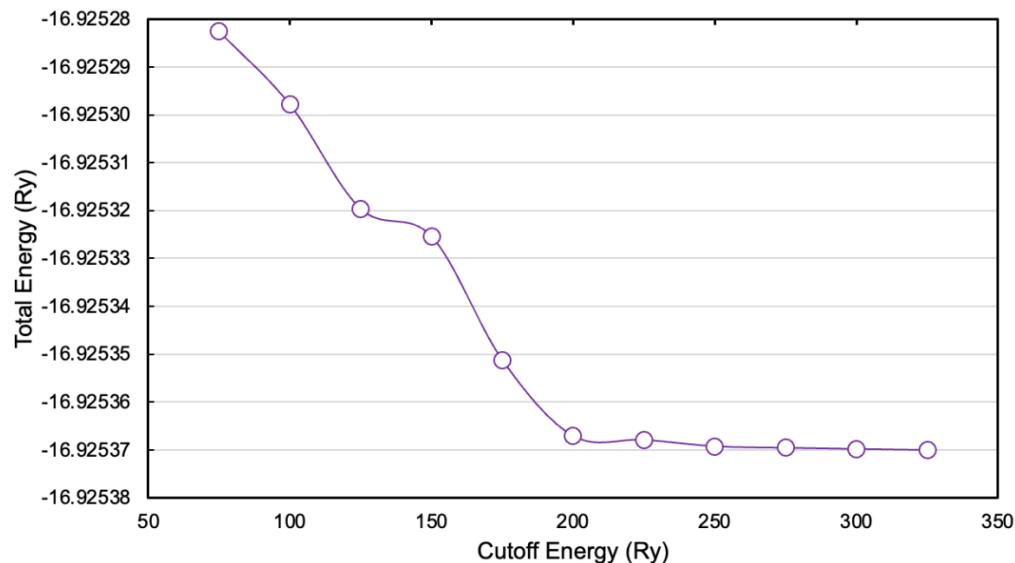


Figure S12. Cutoff energy and energy optimization. By iterating the self-consistent field calculation with varying wavefunction cutoff energies and at fixed convergence thresholds and k -mesh, the convergence of the calculation was found by minimizing the total energy. A 200 Ry cutoff energy was used for all subsequent calculations. See example input files.

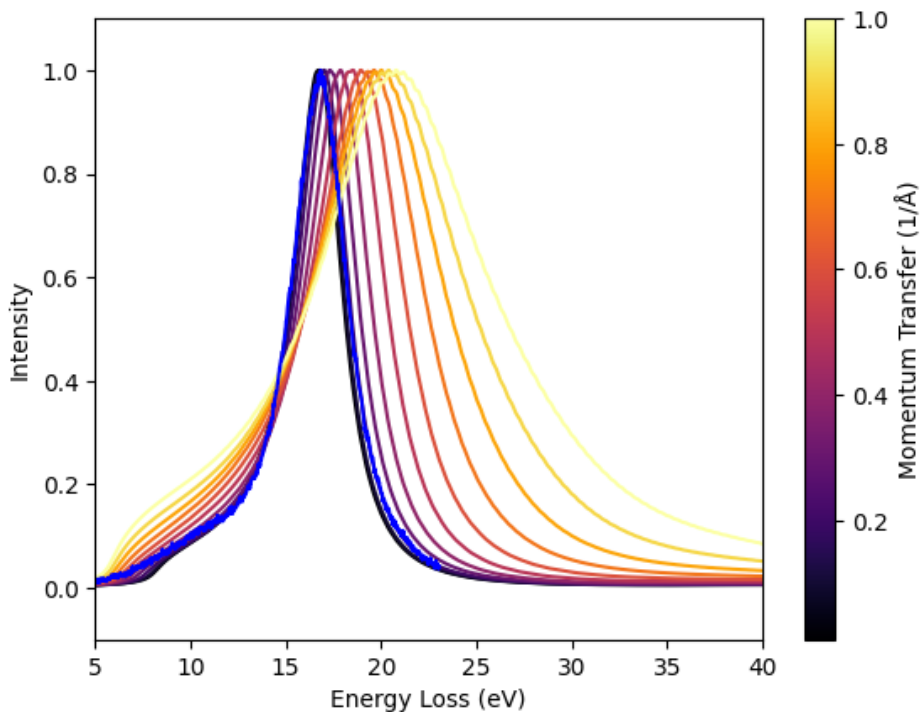


Figure S13. turboEELS momentum dependence. Momentum-dependent turboEELS spectra are compared to the experimental spectrum at the reference temperature (blue).

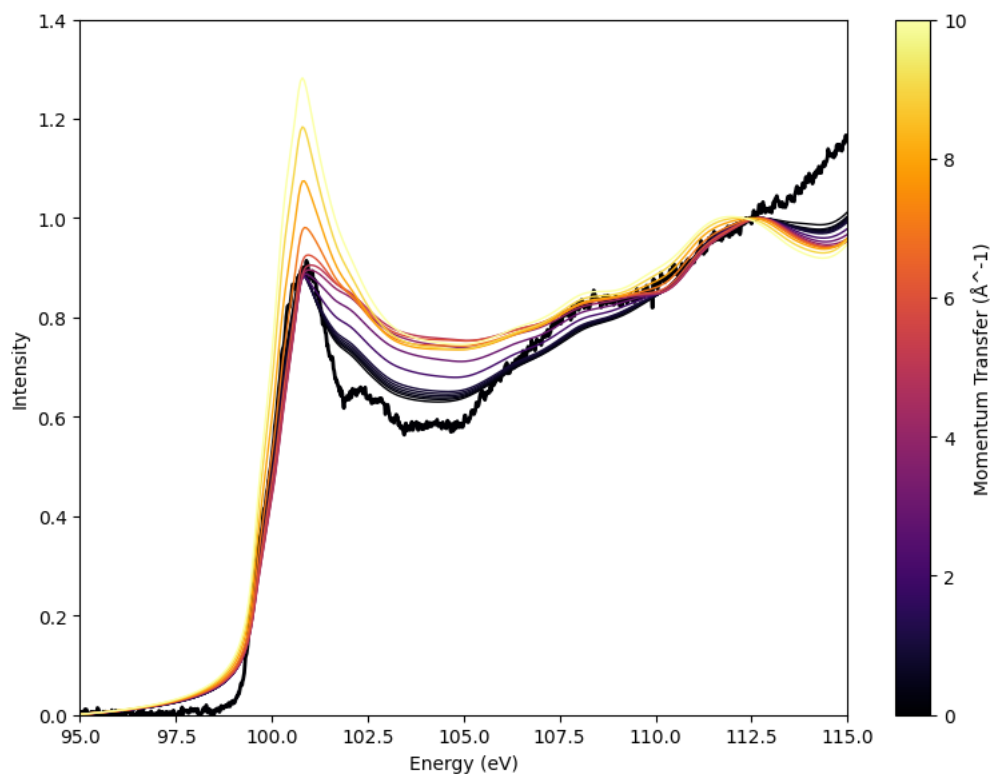


Figure S14. Si L_{2,3} OCEAN momentum dependence. Momentum-dependent OCEAN spectra are compared to the experimental spectrum at the reference temperature (black).

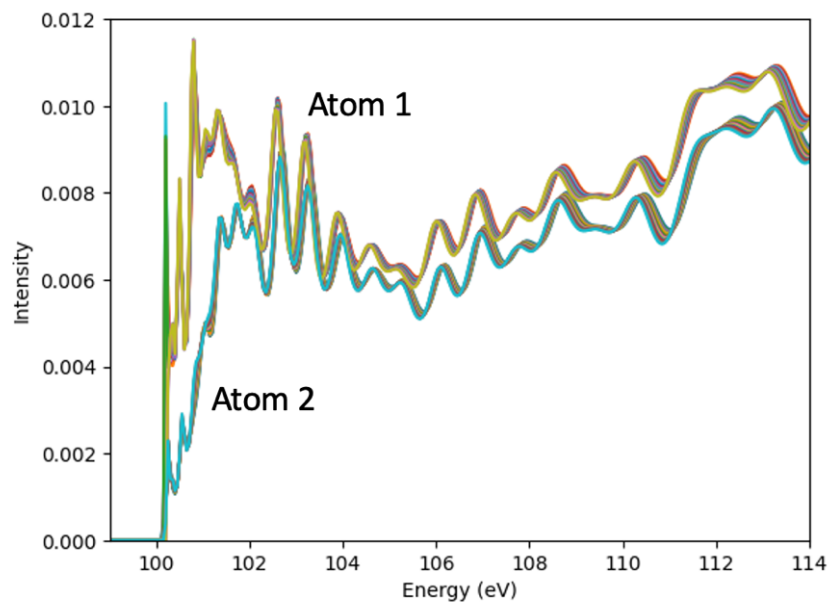


Figure S15. Si L_{2,3} OCEAN atom dependence. There were two atoms in the Si unit cell. To make sure to avoid bias in the data analysis, both atoms were summed and averaged at each temperature.

Scissor Shift Applied to OCEAN Data:

OCEAN SCF gap (eV) [0.6748, 0.6755, 0.6761, 0.6768, 0.6775, 0.6782, 0.674, 0.6789, 0.6796, 0.6803, 0.681, 0.6817, 0.6823, 0.683, 0.6838]

Predicted gap (eV) [1.140000000021464, 1.1317155479213157, 1.1245865472738859, 1.1179564608621686, 1.1115943432100084, 1.1053920357558942, 1.0992926300175108, 1.0932648755234582, 1.0872915832851213, 1.0813634448268268, 1.0754753647586335, 1.0696241704503942, 1.0638071937242035, 1.0580214632278906, 1.0522633477785055]

OCEAN correction (eV): [0.465 0.455 0.445 0.44 0.43 0.425 0.425 0.41 0.405 0.4 0.39 0.385 0.38 0.375 0.365]

Simulated Lattice Parameters (OCEAN and turboEELS):

| a/a0 | a (input Bohr) |
|-------------|-----------------------|
| 0.99986062 | 10.33 |
| 1 | 10.33144 = a0 |
| 1.00013938 | 10.33288 |
| 1.00027876 | 10.33432 |
| 1.00041814 | 10.33576 |
| 1.00055752 | 10.3372 |
| 1.0006969 | 10.33864 |
| 1.00083628 | 10.34008 |
| 1.00097566 | 10.34152 |
| 1.00111504 | 10.34296 |
| 1.00125442 | 10.3444 |
| 1.0013938 | 10.34584 |
| 1.00153318 | 10.34728 |
| 1.00167256 | 10.34872 |
| 1.00181194 | 10.35016 |

Example turboEELS Input File:

STEP 1) pw.x calculation (self-consistent field)

```
&control
  calculation = 'scf'
  prefix = 'si'
  pseudo_dir = './'
  outdir = './out'
  wfcdir = 'undefined'
  tstress = .false.
  tprnfor = true
  wf_collect = .true.
  disk_io = 'low'
/
&system
 ibrav = 2
  celldm(1) = 10.33 ! loops lattice param here!
  nat = 2
  ntyp = 1
  noncolin = .false.
  lspinorb = .false.
  ecutwfc = 200
  occupations = 'fixed'
  smearing = 'gaussian'
  degauss = 0.02
  nspin = 1
  tot_charge = 0
  nosym = false
  noinv = false
  nbnd = 6
/
&electrons
  conv_thr = 1e-10
  mixing_beta = 0.7
  electron_maxstep = 100
  startingwfc = 'atomic+random'
  startingpot = 'atomic'
  diagonalization = 'david'
/
ATOMIC_SPECIES
  Si 28.0855 Si.UPF
ATOMIC_POSITIONS {alat}
  Si 0.00 0.00 0.00
  Si 0.25 0.25 0.25
K_POINTS {automatic}
16 16 16 1 1 1
```

STEP 2) turbo_eels.x calculation (linear-response TDDFT) _____

```
&lr_input
  prefix='si',
  outdir='./out',
  restart_step = 250,
  restart = .false.
/
&lr_control
  itemax = 500,
  q1 = 0.200,
  q2 = 0.000,
  q3 = 0.000,
/
```

STEP 3) turbo_spectrum.x calculation (post-processing the spectrum) _____

```
&lr_input
  prefix='si',
  outdir='./out',
  eels = .true.
  itemax0 = 500
  itemax = 20000
  extrapolation = "osc"
  epsil = 0.03
  units = 1
  start = 0.0d0
  increment = 0.01d0
  end = 50.0d0
  verbosity = 0
/
```

Example OCEAN Input File:

```
#####  
# SETUP  
dft.program { qe }  
computer.para_prefix{ mpirun -n 32 }  
  
# ppdir { './' }  
  
#####  
# DFT AND SCREENING  
dft.ecut 200  
dft.toldfe 1d-10  
dft.tolwfr 1d-10  
dft.den.kmesh{ 16 16 16 } # ngkpt mesh for ground-state calc  
dft.nstep 100  
dft.mixing 0.7  
  
screen.kmesh{ 4 4 4 }  
screen.shells{ 3.5 } # radius for shell for screening  
screen.nbands 100  
  
#####  
# ATOMIC STRUCTURE  
structure.znucl{ 14 }  
structure.typtat{ 1 1 }  
structure.epsilon 11.4 # Static dielectric const  
  
acell{ 10.33 10.33 10.33 }  
structure.rprim{  
0.5 0.5 0.0  
0.5 0.0 0.5  
0.0 0.5 0.5 }  
structure.xred{  
0.00 0.00 0.00  
0.25 0.25 0.25 }  
  
#####  
# BSE AND XAS CALCULATION  
bse.nbands 100  
bse.xmesh{ 6 6 6 }  
bse.kmesh{ 12 12 12 } # nkpt for final state  
bse.core.broaden{ 0.000001 } # Lorentzian broadening (eV)  
  
calc.mode xas  
calc.edges{ -14 2 1 } # Si L23
```